Geochemistry, Geophysics, Geosystems®

AGU ADVANCING EARTH AND SPACE SCIENCES

RESEARCH ARTICLE
10.1029/2025GC012897

Rift Development, Tectonic Forcings, and Magmatic Feedbacks at Santorini and Kolumbo Volcanoes Constrained by Scientific Drilling and Core-Seismic Integration

Jonas Preine[1,2,3], Christian Hübscher[1], Tim Druitt[4], Matthias Hartge[1], Abigail Metcalfe[4], Steffen Kutterolf[5], Katharina Pank[5], Jens Karstens[5], Paraskevi Nomikou[6], Masako Tominaga[2], Emilie Hooft[7], Beck Hufstetler[7], Kaisa Autumn[7], Gareth Crutchley[5], Maria B. Jover[5], Christian Berndt[5], Thomas A. Ronge[8], and IODP Expedition 398 Scientists[9]

[1]Institute of Geophysics, University of Hamburg, Hamburg, Germany, [2]Department of Geology and Geophysics, Woods Hole Oceanographic Institution, Woods Hole, MA, USA, [3]Marine Geoscience, National Oceanography Centre, Southampton, UK, [4]Laboratoire Magmas et Volcans, University Clermont-Auvergne, CNRS, IRD, OPGC, Clermont-Ferrand, France, [5]GEOMAR Helmholtz Centre for Ocean Research Kiel, Kiel, Germany, [6]Department of Geology and Geoenvironment, National and Kapodistrian University of Athens, Athens, Greece, [7]Department of Earth Sciences, University of Oregon, Eugene, OR, USA, [8]Texas A&M University, College Station, TX, USA, [9]See Supplementary Information

Key Points:

- A newly recognized rift structure, the Kolumbo Graben, localizes deformation and volcanism at Santorini and Kolumbo volcanoes
- Deformation rates accelerated after ~330 ka, preceding major explosive volcanism at Santorini and Kolumbo
- Magma ascent preferentially occurred within zones of internal rift deformation rather than along master faults

Supporting Information:

Supporting Information may be found in the online version of this article.

Correspondence to:

J. Preine,
jonas.preine@noc.ac.uk

Citation:

Preine, J., Hübscher, C., Druitt, T., Hartge, M., Metcalfe, A., Kutterolf, S., et al. (2026). Rift development, tectonic forcings, and magmatic feedbacks at Santorini and Kolumbo volcanoes constrained by scientific drilling and core-seismic integration. *Geochemistry, Geophysics, Geosystems*, *27*, e2025GC012897. https://doi.org/10.1029/2025GC012897

Received 16 JAN 2026
Accepted 3 MAY 2026

Author Contributions:

Conceptualization: Jonas Preine, Christian Hübscher, Tim Druitt, Steffen Kutterolf, Paraskevi Nomikou, Thomas A. Ronge
Data curation: Jonas Preine, Christian Hübscher, Tim Druitt, Matthias Hartge, Abigail Metcalfe, Steffen Kutterolf, Katharina Pank, Jens Karstens, Paraskevi Nomikou, Masako Tominaga, Emilie Hooft, Beck Hufstetler, Kaisa Autumn,

Abstract Volcanism in continental rifts, rifted volcanic arcs, and back-arc basins is fundamentally coupled with crustal extension. However, the precise geometry and timing of the fault systems that facilitate magma transport and accommodate extension remain poorly constrained. The Christiana–Santorini–Kolumbo volcanic field lies within the Santorini–Amorgos Tectonic Zone, an actively extending back-arc rift where volcanism transitioned from dominantly effusive and moderately explosive andesitic activity (~570–250 ka) to repeated caldera-forming silicic eruptions after ~250 ka. Here we integrate scientific drilling results from IODP Expedition 398 with a dense grid of high-resolution seismic profiles and identify a previously unrecognized rift structure, the Kolumbo Graben, bounded by the NE–SW–striking Kolumbo Fault and hosting Kolumbo Volcano and the Kolumbo Volcanic Chain. Subsidence and fault throw rates across the rift system accelerated between ~330 and ~160 ka, with the Kolumbo Fault accommodating ~220 m of displacement. This phase of accelerated extension preceded the emergence of Kolumbo and the onset of repeated caldera-forming silicic eruptions at Santorini. Volcanic edifices of the Kolumbo Volcanic Chain cluster within the graben interior rather than along the master fault, indicating that distributed intra-graben deformation and locally reduced horizontal stresses provided preferred pathways for magma ascent. Structural continuity further suggest that the Kolumbo Graben extends beneath Santorini. We conclude that accelerated rifting and strain localization exerted first-order control on magma ascent and the transition to highly explosive volcanism over the past ~250 kyr, while magma intrusion and associated thermal weakening likely provided a positive feedback that further localized deformation during periods of peak activity.

Plain Language Summary Large volcanic eruptions are often linked to stretching of the Earth's crust, but it is not always clear how faults guide magma to the surface. We study this problem at Santorini and the nearby submarine volcano Kolumbo in the southern Aegean Sea. Using detailed seismic images of the subsurface, together with rock and sediment samples drilled by the International Ocean Discovery Program (IODP), we reconstruct how faults and volcanic activity evolved over the past 2 million years. We discover a previously unknown rift structure, the Kolumbo Graben, which formed as crustal stretching became increasingly focused into narrow zones. Fault movement accelerated strongly about 330,000 years ago, just before Santorini began producing its large explosive eruptions and Kolumbo became active. Rather than erupting directly along the main fault, most volcanoes formed above zones of internal deformation within the rift, where the crust was most fractured. Our results show that changes in how the crust stretches can strongly influence where and when volcanoes form and how explosively they erupt.

Gareth Crutchley, Maria B. Jover, Christian Berndt, Thomas A. Ronge
Formal analysis: Jonas Preine, Christian Hübscher, Tim Druitt, Matthias Hartge, Abigail Metcalfe, Steffen Kutterolf, Katharina Pank
Investigation: Jonas Preine, Christian Hübscher, Tim Druitt, Matthias Hartge, Abigail Metcalfe, Steffen Kutterolf, Katharina Pank, Jens Karstens, Paraskevi Nomikou, Masako Tominaga, Emilie Hooft, Beck Hufstetler, Kaisa Autumn, Gareth Crutchley, Maria B. Jover, Christian Berndt, Thomas A. Ronge
Methodology: Jonas Preine, Christian Hübscher, Tim Druitt, Matthias Hartge, Abigail Metcalfe, Steffen Kutterolf, Katharina Pank
Resources: Jonas Preine, Christian Hübscher, Tim Druitt, Jens Karstens, Masako Tominaga, Christian Berndt
Software: Jonas Preine, Christian Hübscher, Matthias Hartge
Validation: Jonas Preine, Christian Hübscher, Tim Druitt, Matthias Hartge, Abigail Metcalfe, Steffen Kutterolf, Katharina Pank
Visualization: Jonas Preine, Matthias Hartge
Writing – original draft: Jonas Preine
Writing – review & editing: Jonas Preine, Christian Hübscher, Tim Druitt, Matthias Hartge, Abigail Metcalfe, Steffen Kutterolf, Katharina Pank, Gareth Crutchley, Maria B. Jover, Christian Berndt

1. Introduction

Volcanism in extensional tectonic settings can produce hazardous large-scale eruptions, particularly in continental rifts, rifted volcanic arcs, and back-arc regions (Hughes & Mahood, 2011). Prominent examples include the East African Rift (Rooney et al., 2025), the Taupō Volcanic Zone (Wilson et al., 2009), the Basin and Range Province (Valentine & Perry, 2007), the Ryukyu Arc (Mahony et al., 2011), the Campanian Volcanic Province (Rolandi et al., 2003), and the South Aegean Volcanic Arc (Metcalfe et al., 2025a), where complex interactions between volcanism and faulting have been documented. In volcanic arc settings, mantle melting is triggered by fluid release from the subducting slab (Stern, 2002), whereas in continental rift and back-arc settings, extension of the crust causes decompression of the underlying asthenosphere that can induce partial melting of the mantle (Brown et al., 1995; Sternai, 2020). These processes result in the formation of magma bodies at the base of, or within, the crust (Ruppel, 1995). Extensional faults can increase the permeability of the crust immediately surrounding the fault, creating potential pathways for magma migration from deeper reservoirs to the surface. Determining the temporal interaction between faulting and magmatism, and the structure of fault systems that contribute to volcanic eruptions, is crucial to understanding the magmatic and tectonic dynamics of active volcanic regions and to improving predictions of the sites of future eruptions (Biggs et al., 2021).

Here, we develop an unprecedented data set that enables the spatio-temporal reconstruction of fault-controlled volcanism within the Christiana–Santorini–Kolumbo volcanic field of the southern Aegean Sea (Figure 1a). This region provides a natural laboratory to investigate how rifting interacts with the plumbing system of a multicyclic caldera complex over several hundred thousand of years (Kokkalas & Aydin, 2013; Metcalfe et al., 2025a; Pe-Piper & Piper, 2005; Preine, Hübscher, et al., 2022). The Christiana-Santorini-Kolumbo volcanic field occupies the central part of the South Aegean Volcanic Arc (Figure 1a) and has experienced at least four silicic caldera-forming eruptions within the past 200 thousand years, the most recent being the Minoan eruption 3.6 kyr ago (Druitt et al., 1999). Subsequent volcanic activity produced the Kameni Volcano within the Santorini caldera, including an explosive eruption in 726 CE (Preine et al., 2024; Pyle & Elliott, 2006). To the northeast, the submarine Kolumbo Volcano forms the largest edifice of the Kolumbo Volcanic Chain, a system of more than 20 submarine edifices (Carey et al., 2013; Nomikou et al., 2013) (Figures 1b and 1c). Kolumbo has been active since ∼265 ka (Metcalfe et al., 2026) and its most recent eruption in 1650 CE generated a tsunami that inundated nearby islands and caused numerous casualties (Karstens et al., 2023a; Ulvrova et al., 2016).

The Kolumbo Volcanic Chain strikes NE–SW, parallel to the major basin structures of the Santorini–Amorgos Tectonic Zone (SATZ), which is defined by NE–SW oriented half-grabens and asymmetric grabens bounded by major extensional faults (Nomikou et al., 2018; Preine, Hübscher, et al., 2022) (Figures 1b and 1c). Santorini is located near the intersection of an older E–W Pliocene rift system and the younger NE–SW Pleistocene rift system (Heath et al., 2019; Pe-Piper & Piper, 2007; Preine, Hübscher, et al., 2022), and while earlier studies proposed a basin extending beneath Santorini (Budetta et al., 1984; Heath et al., 2019; Heiken & McCoy, 1984), no major (>100 m) faults have been documented in the subaerial caldera walls (Druitt et al., 1999) or have been identified in adjacent seismic data (Preine, Hübscher, et al., 2022). Instead, a complex fault termed the *Kolumbo Fault*, has been identified near Santorini, forming a blind normal fault zone with relay ramps about 6 km northwest of Kolumbo (Crutchley et al., 2023). The apparent absence of major tectonic structures near Santorini and Kolumbo led earlier studies to propose that magmatism may have accommodated much of the local strain within the volcanic basins (Preine, Hübscher, et al., 2022).

The need for a holistic understanding of interactions between rift tectonics and magmatism, and their hazard implications, came to the fore most recently during the 2025 seismic crisis at Santorini. In late January 2025, an intense earthquake swarm began with tens of thousands of earthquakes up to magnitude 5 occurring beneath the Anhydros Ridge (Isken et al., 2025; Lomax et al., 2025) (Figure 1b), leading to partial evacuations of Santorini. The swarm originated at a depth of ∼12–15 km and was interpreted as a dike intrusion from Kolumbo's mid-crustal reservoir, propagating northeastwards and parallel to the major tectonic structures of the SATZ (Isken, Karstens et al., 2025; Lomax et al., 2025). The main phase of the swarm continued for over 30 days. While it did not lead to an eruption, the earthquake sequence highlighted the need for a comprehensive model that links the tectonic and volcanic systems to better understand the potential location of future eruptions.

A major challenge in reconstructing volcano–tectonic feedbacks is that the stratigraphic record commonly integrates signals from both tectonic deformation and volcanic deposition (Metcalfe et al., 2025a). In many rift basins, accommodation space is filled progressively by syn-tectonic sedimentation, allowing subsidence histories

10.1029/2025GC012897

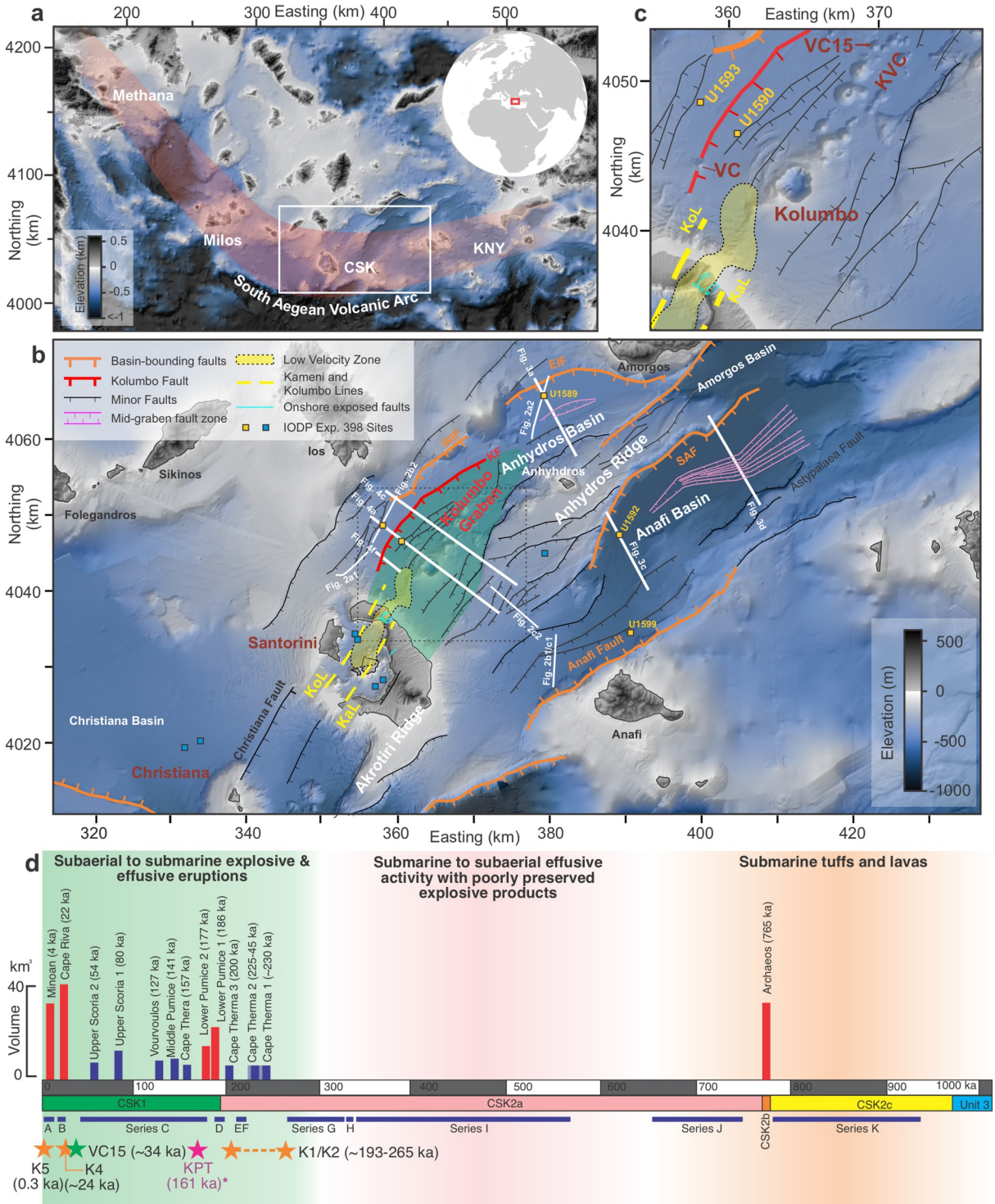

Figure 1.

to be reconstructed from thickness variations (Gawthorpe & Leeder, 2000). However, in volcanic rift systems such as the SATZ, rapid emplacement of thick volcaniclastic deposits can obscure or overprint tectonic signals, making it difficult to determine whether basin deepening precedes, accompanies, or follows volcanic activity.

In this study, we investigate the interplay between tectonic faults and the volcanic behavior of Santorini and Kolumbo by integrating high-resolution multichannel seismic data with core-constrained stratigraphy from IODP Expedition 398. Our objectives are to (a) re-assess the seismostratigraphic framework surrounding the Kolumbo Volcanic Chain and Santorini, (b) disentangle tectonic and volcanic contributions to basin evolution, (c) and investigate potential tectonic-magmatic coupling mechanisms at this highly active volcanic system.

2. Geological Framework

The Christiana-Santorini-Kolumbo volcanic field lies in the center of the South Aegean Volcanic Arc, which formed due to subduction of the African plate beneath Eurasia (Le Pichon & Angelier, 1979; Royden & Papanikolaou, 2011). Since the Late Miocene, rollback of the African slab, gravitational collapse of overthickened crust, westward motion of Anatolia, and slab tears beneath the eastern Aegean and Anatolia have driven southward retreat of the arc and internal deformation of the Aegean microplate (Jolivet, 2001; Le Pichon & Angelier, 1979; Le Pichon & Kreemer, 2010). These processes created the present-day horst-and-graben morphology of the Cyclades (Le Pichon & Kreemer, 2010; Royden & Papanikolaou, 2011), where crustal thickness is reduced to 20–30 km compared to 40–50 km beneath mainland Greece and Turkey (Zhu et al., 2006). Extension has been long-lived and polyphase. N–S extension in the Miocene–Pliocene generated E–W striking listric faults and basin subsidence (Anastasakis & Piper, 2005; Pe-Piper & Piper, 2007). Progressive increase in curvature of the arc in the Pliocene–Pleistocene introduced counterclockwise block rotations and was accommodated by new NE–SW striking fault systems (Gautier & Brun, 1999; Papazachos, 2019; van Hinsbergen & Schmid, 2012). Among these fault systems is the prominent NE-SW oriented rift system of the SATZ which is 100 km long and 45 km wide, situated in the back-arc of the South Aegean Volcanic Arc (Figure 1b) (Nomikou et al., 2018).

The SATZ comprises NE–SW striking, en-echelon basin structures, including the Anhydros, Anafi, and Amorgos basins, which contain >1 km of sediment and are bounded by major extensional faults with throws exceeding 2 km (Figure 1b) (Hooft et al., 2017; Nomikou et al., 2018; Preine et al., 2020). To the southwest, the Christiana Basin represents an older E–W fault system subsequently overprinted by neotectonic NE–SW faults that may continue beneath Santorini (Figure 1b) (Heath et al., 2019; Preine, Hübscher, et al., 2022). Alongside this evolving tectonic framework, the Christiana-Santorini–Kolumbo volcanic field developed as the central segment of the South Aegean Volcanic Arc, active since 3–4 Ma (Nomikou et al., 2013; Pe-Piper & Piper, 2007). The Christiana-Santorini-Kolumbo volcanic field comprises the extinct Christiana volcanic center, Santorini, Kolumbo, and the Kolumbo Volcanic Chain (Nomikou et al., 2019; Preine, Hübscher, et al., 2022), which are located at the intersection of the Christiana Basin and the western Anhydros Basin (Figure 1b) (Heath et al., 2019; Preine, Hübscher, et al., 2022).

Figure 1. Morphology of the Santorini-Amorgos Tectonic Zone and eruption history of Santorini and Kolumbo. (a) Regional map of the southern Aegean Sea showing the South Aegean Volcanic Arc (shaded red). The white box marks the study area. The coordinate system here and in subsequent maps is UTM Zone 35N, WGS84 datum. CSK: Christiana-Santorini-Kolumbo. KNY: Kos-Nisyros-Yali. (b) Morphological map of the Santorini-Amorgos Tectonic Zone. Orange squares show IODP Expedition 398 sites relevant to this study. Blue squares indicate other IODP Expedition 398 drill sites. Major basin-bounding faults are indicated by orange lines (Nomikou et al., 2018) (SAF: Santorini–Anafi Fault, WIF: West Ios Fault; EIF: East Ios Fault) minor faults are illustrated in black (modified from Nomikou et al. (2018) and Isken et al. (2025) and mapped in this study). The red line indicates the Kolumbo Fault (KF). Semi-transparent green area indicates the extent of the Kolumbo Graben in the western Anhydros Basin. Yellow dashed lines indicate the Kolumbo (KoL) and Kameni lines (KaL) (Druitt et al., 1999; Heath et al., 2019). Semi-transparent yellow area locates the shallow low-velocity zone from McVey et al. (2020). Light blue lines indicate onshore exposed faults (Druitt et al., 1999; Drymoni et al., 2022). Pink lines indicate the extent of mid-graben fault zones. White lines indicate seismic profiles shown in Figures 2–4. A map showing all available multi-channel seismic lines is provided in Figure S1 in Supporting Information S1. Bathymetry and elevation data modified from Nomikou et al. (2013, 2018) and Hooft et al. (2017). (c) Close up of Santorini, Kolumbo and the Kolumbo Volcanic Chain (KVC). VC: Volcanic Cone. KoL: Kolumbo Line. KaL: Kameni Line. (d) Eruptive history of NE Santorini and Kolumbo showing the main eruptions represented in the IODP cores (Metcalfe et al., 2025a, 2025b, 2026). Previously known onland eruptions (Druitt et al., 1999) are shown as vertical bars scaled to dense-rock equivalent volume (Druitt et al., 2024a; Karstens et al., 2023a; Kutterolf, Freundt, Druitt, et al., 2021; Metcalfe et al., 2025a); caldera-forming silicic eruptions are in red, other explosive eruptions in blue. Newly identified volcanic layers from the IODP cores are indicated by blue bars labeled A–K (Metcalfe et al., 2025a, 2026). Eruptions from Kolumbo are marked by orange stars (Metcalfe et al., 2026). Green star indicates eruption age of VC15 from the KVC (Vougioukalakis et al., 2025). The pink star indicates the Kos Plateau Tuff (Metcalfe et al., 2025b; Smith et al., 1996). Ages of seismostratigraphic units are shown by the horizontal bars (CSK1-3).

Scientific drilling results from IODP Expedition 398, combined with radiometric dating of lavas from Christiana (Vroon et al., 2025) show that Christiana Volcano is significantly older (2.5–2.7 Ma) than Santorini–Kolumbo (<1 Ma). Santorini's geological history is divided into Ancient Santorini (~940–570 ka, mostly erupting amphibole-bearing rhyolites) and Modern Santorini (<570 ka, largely erupting amphibole-scarce basalt to rhyodacite; Metcalfe et al., 2025a, 2026). At ~765 ka, Ancient Santorini produced the major Archaeos explosive eruption, whose deposits provide a distinctive seismic marker in the surrounding basins (Figure 1d) (Druitt et al., 2024a; Preine, Karstens, Hübscher, Crutchley, et al., 2022). Between 570 and 250 ka, Modern Santorini was characterized by effusive to moderately explosive stratovolcano-like activity (Figure 1b) (Metcalfe et al., 2025a, 2026). Around 250 ka, the system entered a new regime marked by the Thera Pyroclastic Formation, consisting of two cycles of explosive eruptions, each culminating in paired caldera-forming silicic eruptions (CFSE) (Lower Pumice 1 (186 ka) and Lower Pumice 2 (177 ka); Cape Riva (22 ka) and Minoan (3.6 ka); Druitt et al., 1999; Kutterolf, Freundt, Druitt, et al., 2021; Wulf et al., 2020) (Figure 1d). Volcanism during that time was mainly confined to the northern caldera basin, bounded by two lineaments, the Kameni and Kolumbo Lines (Druitt et al., 1999), which also bound a shallow low-velocity anomaly interpreted as an active magma reservoir (Figure 1c) (Heath et al., 2019; Hooft et al., 2019; McVey et al., 2020). The Thera Pyroclastic Formation today forms much of the southern caldera cliffs of Santorini and thick volcaniclastic deposits in the surrounding basins (Karstens et al., 2023b; Metcalfe et al., 2025a; Preine, Hübscher, et al., 2022). Santorini's most recent caldera-forming eruption, the Minoan eruption (~3.6 ka) erupted 34.5 ± 6.8 km^3 of magma (Karstens et al., 2023c).

Kolumbo, northeast of Santorini, is fed by a small, shallow silicic reservoir at 2–5 km depth that sustains vigorous, high-temperature hydrothermal venting and recurrent microseismic swarms (Chrapkiewicz et al., 2022; Schmid et al., 2022). It is linked to a mid-crustal magma reservoir located ~5–10 km southeast of the edifice at 11–13 km depth containing ~10%–15% of melt (Autumn et al., 2025; Hufstetler et al., 2025). Seismic reflection data distinguish five eruptive units at Kolumbo (K1–K5), the uppermost unit K5 corresponding to the 1650 CE eruption (Hübscher et al., 2015; Karstens et al., 2023b). Marine tephra layers recovered during IODP Expedition 398 record at least 19 eruptions from Kolumbo ranging in composition from basaltic andesite to rhyolite beginning at ~265 ka (Metcalfe et al., 2026). These results place the earliest activity of Kolumbo (K1/K2) between ~265 and 193 ka and a younger phase (K4/K5) between 24 and 0.4 ka (Metcalfe et al., 2026). Seismostratigraphic relationships indicate that K3 erupted during Santorini's Middle Tuff Sequence (the period from 177 to 22 ka) but since it is much smaller than the other eruptive units of Kolumbo, we don't further consider it here (Preine, Hübscher, et al., 2022). $^{39}Ar/^{40}Ar$ ages of lava lithics from within submarine crater exposures of the 1650 CE deposits yield ages of 202.9 ± 36.9, 217.6 ± 24.9, and 247.1 ± 44.7 ka that may be linked to the K1/K2 seismic unit (Vougioukalakis et al., 2025). To date, only one cone of the Kolumbo Volcanic Chain (cone VC15) has been dated, yielding an age of 34.2 ± 15.7 ka (Vougioukalakis et al., 2025).

The many explosive eruptions of Santorini and Kolumbo laid down tephra layers in the surrounding marine basins that have been sampled, chemically fingerprinted, and correlated between drill sites and with onland eruption deposits (Metcalfe et al., 2025a, 2025b, 2026). While many of the cm-to-dm-thick tephras were emplaced as fallout, those from the CFSE eruptions of Santorini and the largest explosive eruptions of Kolumbo form volcaniclastic megabeds many meters, tens of meters, or in one case >200 m thick. From their great thicknesses and bathymetry-filling nature, these submarine megabeds are interpreted mainly as the products of instantaneously emplaced submarine gravity flows formed by the entry of large-volume pyroclastic currents into the sea (Druitt et al., 2024a, 2024b, 2024c, 2024d, 2024e; Metcalfe et al., 2025a, 2025b, 2026).

The volcanic evolutions of Santorini and Kolumbo have been linked to regional tectonic activity (Metcalfe et al., 2025a, 2026; Preine, Hübscher, et al., 2022). Previous studies proposed that the SATZ experienced one or more phases of accelerated rifting, described as "rift pulses," prior to the formation of the Thera Pyroclastic Formation at Santorini (Preine, Hübscher, et al., 2022). Evidence for such pulses was based on prominent onlap surfaces in the East Anafi and Anhydros Grabens (Hübscher et al., 2015; Preine, Hübscher, et al., 2022). These onlap geometries contrast with expectations from continuous hanging-wall rotation, where syn-tectonic sedimentation keeps pace with subsidence and produces divergent internal reflections. Instead, each sharp onlap surface was interpreted to record a short-lived interval of rapid subsidence during which sedimentation lagged behind, generating a regionally traceable onlap surface rather than typical syn-rift geometries (Preine, Hübscher, et al., 2022).

Subsequent results from IODP Expedition 398 showed that the most pronounced onlap surface (called csk1; see below) corresponds to a major shift from mainly marine sedimentation in potentially starved rifts to rapid, near-instantaneous infilling by thick volcanic megabeds (Metcalfe et al., 2025a). This complicates tectonic interpretations, as it implies that thickness variations and onlap behavior alone are not reliable indicators for the timing of subsidence: they do not resolve when accommodation was created, nor allow us to reliably access whether extension occurred synchronously with sedimentation. It also challenges standard subsidence-reconstruction techniques (e.g., structural restoration; Nunns, 1991), which assume (a) progressive infill leading to a flat seafloor at any given time and (b) onlap primarily reflecting tectonically generated accommodation. Neither assumption holds in the SATZ, where the results of IODP Expedition 398 show that the major grabens potentially acted as starved rifts, and the regionally traceable csk1 onlap surface is most importantly a lithological transition, not necessarily a tectonic one (Metcalfe et al., 2025a).

To explain the relationship between onlap surfaces in the rift basins and the onset of CFSE volcanism at Santorini, two conceptual models were proposed by Metcalfe et al. (2025a) to explain this relationship:

Model 1 attributes the Modern Santorini's transition to CFSE activity to internal magmatic evolution, independent of tectonics. In this interpretation, continuous subsidence simply deepened the basins into bathymetric troughs. When Santorini entered its highly explosive phase, pyroclastic currents flowed into these troughs and generated thick, onlapping megabed successions, analogous to valley-filling ignimbrite emplacement on land (e.g., Cas et al., 2024). In this scenario, the seismically imaged onlap surfaces reflect depositional geometry rather than tectonically driven basin reorganization.

Model 2 proposes that the transition to caldera-forming silicic explosive (CFSE) activity was driven by prolonged regional extension and a phase of rapid rift subsidence and basin deepening between ∼300 and 250 ka. In this interpretation, rifting enhanced the flux of mantle-derived melts, heat, and fluids into the transcrustal magmatic system, increased melt percolation through crustal reservoirs, and reorganized magma storage architecture, collectively amplifying internal magmatic processes and promoting explosive volcanism. Regional tectonic forcing, rather than magmatism triggering rifting, is favored.

These two models represent end-member scenarios. In reality, tectonic and volcanic forces likely interacted through a self-reinforcing feedback loop, where the dominance of one process over the other may have shifted over time. It is well established that lithospheric stretching can increase magma production (Fioraso et al., 2024; Sternai, 2020), while conversely, the intrusion of magma into the crust weakens the lithosphere, facilitating further and faster extension (Brune et al., 2023; Buck, 2004). While Metcalfe et al. (2025a) argued for a dominance of tectonic forcing on the magmatic system of Santorini and Kolumbo (Model 2), direct evidence for rift acceleration has been lacking so far, as previous constraints of basin deepening come from the eastern Anafi and Anhydros Basins, located several tens of kilometers to the NE of Santorini and Kolumbo (Figure 1b), leaving the spatial relationship of rifting to the volcanic system unclear. Consequently, spatio-temporal evidence for accelerated rifting immediately prior to the broadly synchronous onset of CFSE volcanism at Santorini and emergence of Kolumbo remains elusive.

3. Methods

3.1. Reflection Seismic Data

Multichannel reflection data for this study were acquired during four expeditions (POS338, POS538, MSM132, and MSM135), with parameters tuned per survey (Figure S1 in Supporting Information S1). Acquisition specifics are: (a) POS338 (2006, R/V Poseidon)—GI gun in true GI mode (45/105 in^3), 24-channel analog streamer (600 m), CMP spacing 12.5 m; dominant frequency ∼60 Hz yielding ∼8–15 m vertical resolution (Hübscher et al., 2006); (b) POS538 (2019, R/V Poseidon)—GI gun in harmonic mode (45/45 in^3), concatenated GeoEel streamer (active 190–250 m), CMP spacing ∼1.56 m; dominant frequency ∼125 Hz, vertical resolution ∼4–8 m (Karstens et al., 2020); (c) MSM132 (2025, R/V Maria S. Merian)—configuration 1: two GI guns (harmonic 75/75 in^3; harmonic 45/45 in^3) and a 125 m digital GeoEel streamer (80 channels, 1.5625 m group interval), configuration 2: GI gun (harmonic 75/75 in^3) and a 75 m digital GeoEel streamer (48 channels, 1.5625 m group interval). CMP spacing 1.5625 m, 0.5 ms sampling; dominant frequency ∼125 Hz, vertical resolution ∼4–8 m (Berndt et al., 2025); (d) MSM135 (2025, R/V Maria S. Merian) two GI guns (harmonic 105/105 in^3; true GI 45/

105 in^3), digital Hydroscience Seamux streamer (450 m active, 108 channels, 4.17 m group), CMP spacing 4.17 m, 1 ms sampling; dominant frequency ∼100 Hz, vertical resolution ∼5–10 m (Hübscher et al., 2025).

Processing was performed in VISTA and comprised trace editing, band-pass/Ormsby filtering (low-cut where specified), predictive deconvolution where applicable, surface-related multiple elimination (for data from Expeditions POS338, POS538 and MSM135), spherical divergence correction, velocity analysis with normal moveout correction, common midpoint stacking, finite-difference or Kirchoff migration, time-variant filtering, top mute, and residual noise suppression. Interpretation and mapping were performed using KingdomSuite. To characterize the geometry of the Kolumbo Fault, we produced a depth-converted seismic section across the fault zone. Because strong lateral velocity heterogeneities prevented the use of a robust velocity model for full depth migration, we instead applied simple, averaged interval velocities derived from IODP Expedition 398 to stretch the time-migrated section into depth. Although this approach does not replace true depth migration, it provides a realistic first-order approximation of subsurface structure.

3.2. Age Model Construction and Core-Seismic Integration

During IODP Expedition 398, 12 sites were drilled in and around Christiana, Santorini and Kolumbo, four within the Santorini caldera and eight in the surrounding rift basins (Druitt et al., 2024b). We focus on the drill sites located northeast of Santorini within the Anhydros and Anafi Basins (Sites U1589, U1590, U1592, U1593; Figures 1b and 1c), which together capture the volcano-sedimentary infill of the SATZ. Core descriptions, physical properties, and shipboard biostratigraphic age models were obtained following standard IODP protocols (Kutterolf et al., 2024a). Samples of individual tephra and pumice layers were analyzed for glass-shard major and trace element compositions by electron microprobe and Laser Inductively Coupled Plasma Mass Spectrometry for correlation and fingerprinting purposes (Druitt et al., 2024a; Metcalfe et al., 2025a, 2025b, 2026). Biostratigraphic ages were derived from calcareous nannofossil and planktonic foraminiferal assemblages at one sample per ∼5–10 m, complemented by age control from sapropel horizons of known Mediterranean age (Rohling et al., 2015). Tephra ages were established through chemical correlation with dated marine tephras from shallow gravity cores (Kutterolf, Freundt, Hansteen, et al., 2021; Wulf et al., 2020) and, where possible, by ^{40}Ar-^{39}Ar and U-Pb zircon geochronology (Beethe et al., 2025; Druitt et al., 2024a). For further details refer to Druitt et al. (2024a) and Metcalfe et al. (2025a, 2025b, 2026).

Core–seismic integration followed the workflow of Preine et al. (2025). Shipboard P-wave velocity and bulk-density measurements from whole- and half-round cores were filtered and interpolated to generate acoustic impedance logs and synthetic seismograms. These were correlated with extracted traces from high-resolution multichannel seismic profiles to establish time–depth conversions and tie-points at each site. The quality of each tie was evaluated by the alignment of lithologic boundaries and prominent seismic reflectors.

4. Results

4.1. Ground-Truthed Seismostratigraphy

We adopt and extend the published seismo- and chronostratigraphic framework established from reflection-seismic data correlated to IODP Expedition 398 drill cores (Preine et al., 2025; Druitt et al., 2024a; Metcalfe et al., 2025a, 2025b, 2026) and extend it across the study area. We use crossing and adjacent seismic lines by means of jump correlations to extend the stratigraphy of the Anhydros and Anafi basins. Across our study area, we distinguish three main seismostratigraphic units (CSK1–CSK3), separated by unconformities or correlated conformities, labeled csk1–csk3 (Figure 2).

Unit CSK1 is dominated by silicic lapilli ashes and oozes with multiple ash beds (Druitt et al., 2024b) and contains the deposits of CFSE of Modern Santorini spanning from ∼186 ka to the present day (Figure 2a). It incorporates products of onshore-known eruptions, such as the Minoan (3.6 ka), Cape Riva (22 ka), and the 177–22 ka Middle Tuff Sequence (here defined as all tephras between the Cape Riva and Lower Pumice 2 eruptions, including Upper Scoria 2 (54 ka), Upper Scoria 1 (81 ka), Middle Pumice (141 ka), and Cape Thera (157 ka) eruptions), Lower Pumice 2 (177 ka) and Lower Pumice 1 (186 ka) eruptions, as well as newly identified tephras from IODP Expedition 398 (from Metcalfe et al., 2025a, updated by Metcalfe et al., 2026), including Tephra A (1.5 ka), Tephra B (24 ka; renamed Kolumbo Tephra 3 by Metcalfe et al., 2026), and Tephra Series C (185–45 ka). The base of Unit CSK1 is defined by the base of the Lower Pumice 1 eruption (Figure 2a) (Metcalfe et al., 2025a).

a

Unit	Age Bracket	Contained Eruptive Products	Sampled Lithologies	Seismic Character	P-Wave Velocity
CSK1	volcanic: ~186 ka–0 ka	Kolumbo K5 (1650 CE) Tephra A (1.5 ka) Minoan (3.6 ka) Cape Riva (22 ka) Kolumbo K4 (~24 ka) Tephra B (24 ka) Tephra series C (45-185 ka) VC15 (34 ka) Kolumbo K3 (*~30-40 ka?*) Middle Tuff Sequence (22-177 ka) Kos Plateau Tuff (161 ka) Lower Pumice 2 (177 ka) Lower Pumice 1 (186 ka)	Silicic lapilli ashes, Oozes with multiple ashes	Subparallel reflections of moderate to high amplitudes intercalated with chaotic to transparent subunits; systematic thickening toward basin faults; onlap at base csk2a.	1618 ± 78 m/s

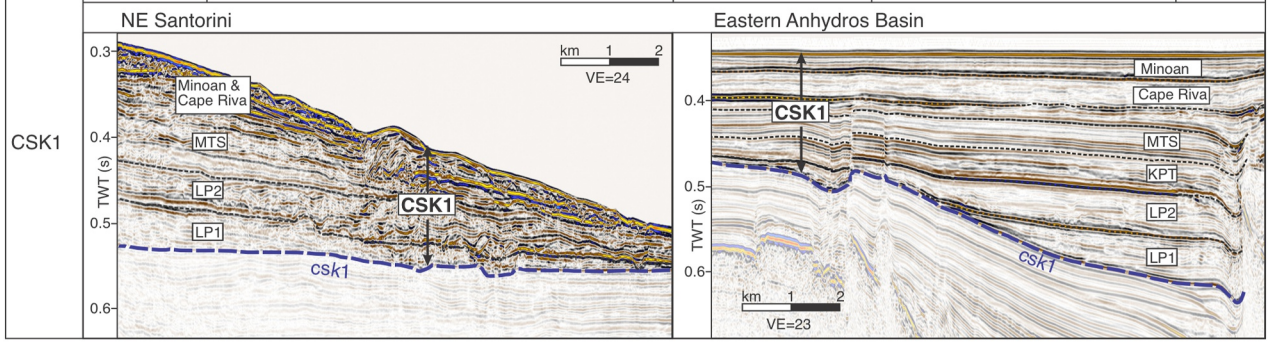

b

Unit	Age Bracket	Contained Eruptive Products	Sampled Lithologies	Seismic Character	P-Wave Velocity
CSK2	volcanic: 189–940 ka; biostrat: 470–610 ka	Tephra D (189 ka), Cape Therma 3 (200 ka) Kolumbo K2/K1 (193-265 ka) Tephra E (209 ka) Tephra F (210 ka) Cape Therma 1 (230 ka) Tephra series G (265-330 ka) Tephra H (330 ka) Tephra series I (330-570 ka) Tephra series J (645-750 ka) Archaeos Tuff (~765 ka) Tephra Series K (775-940 ka)	**CSK2a**: Oozes with multiple ashes. **CSK2b**: Lapilli-ash (Archaeos). **CSK2c**: Thin to moderate volcanic beds.	**CSK2a**: Well-stratified, medium-amplitudes, laterally continuous. **CSK2b**: Distinctive, regionally traceable megabed; chaotic to weakly transparent internal character. **CSK3b**: Chaotic to semi-transparent subunits; bounded by high-amplitude reflectors	1694 ± 133 m/s

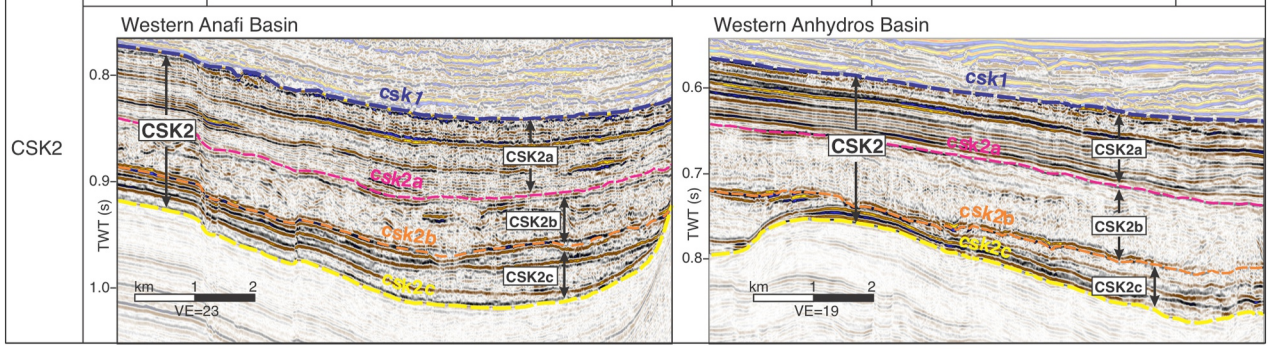

c

Unit	Age Bracket	Contained Eruptive Products	Sampled Lithologies	Seismic Character	P-Wave Velocity
CSK3	biostrat: ~0.97 - >2 Ma		Oozes with rare ash, dolomitic sands (U1592), conglomerates (U1589), sandstones (U1599).	Well-stratified, medium amplitude, partly chaotic reflections.	1920 ± 372 m/s

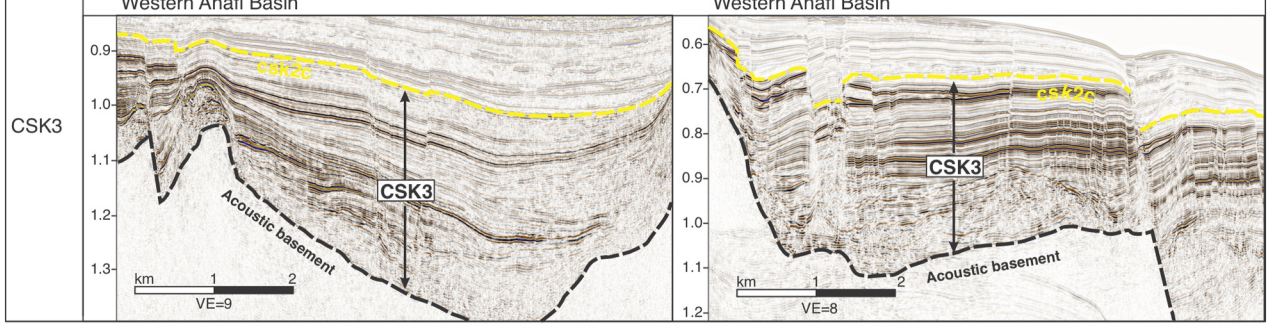

Figure 2. Ground-truthed seismostratigraphic units for the Santorini-Amorgos Tectonic Zone. Volcanic ages and contained eruptions are based on Druitt et al. (2024a) and Metcalfe et al. (2025a, 2025b, 2026). Biostratigraphic ages and average p-wave velocities are based on the shipboard analyses from IODP Expedition 398 (Druitt et al., 2024b). VE: Vertical Exaggeration. Locations of the displayed profiles are shown in Figure 1 (panel 1 is on the left and panel 2 on the right).

Also contained within this unit are the Kos Plateau Tuff (161 ka), forming a massive to diffusely stratified deposit exceeding 200 m thickness in the Anafi Basin (Metcalfe et al., 2025b), and the upper units from Kolumbo (K4–K5; ~24–0.4 ka) (Metcalfe et al., 2026), including the dated edifice VC15 of the Kolumbo Volcanic Chain (Vougioukalakis et al., 2025). Because of upward reworking, all biostratigraphic age markers from Expedition 398 are disregarded in Unit CSK1 (Metcalfe et al., 2025a, 2025b, 2026).

Unit CSK1 is expressed seismically as a sequence of chaotic, high-amplitude reflections proximal to Santorini and Kolumbo, transitioning to weakly reflective facies in the distal basins, where the unit thickens toward basin-bounding faults (Figure 2a). The transition from chaotic proximal reflections to weakly reflective distal facies reflects a dominance of volcaniclastic gravity-flow deposits, which are highly sensitive to bathymetric lows and result in rapid, topographically controlled infilling of the grabens (Metcalfe et al., 2025a, 2025b). Onlap terminations occur toward unconformity csk1 in the grabens, whereas away from them the boundary is generally conformable. Based on core–seismic integration, we are able to identify and trace major eruptive units in the seismic data throughout most of the study area. Traceable internal units include the Minoan, Cape Riva, Middle Tuff Sequence, Kos Plateau Tuff, Lower Pumice 2, and Lower Pumice 1 deposits (Figure 2a), representing individual fining-upward deposits with high-acoustic impedance contrasts at their top and base (Manga et al., 2025). In the eastern Anhydros Basin, these occur as laterally extensive megabeds with incoherent, low-amplitude internal reflections separated by prominent high-amplitude boundaries. A notable exception is the Middle Tuff Sequence, which exhibits more continuous, medium-amplitude reflections and greater internal stratification (Figure 2a). The eastern Anafi Basin is dominated by an exceptionally thick (~200 m) deposit of the Kos Plateau Tuff, accompanied by traceable deposits of the Minoan, Cape Riva, Lower Pumice 2 and Lower Pumice 1 eruptions (Metcalfe et al., 2025a, 2025b, 2026). The Kos Plateau Tuff megabed is characterized by generally low-amplitude reflections with internal stratification and distinct reflection contrasts, including a prominent internal boundary marking a transition from coarse-grained ash in the lower part to finer ash above (Metcalfe et al., 2025b). Its basal surface forms a sharp, high-amplitude reflection, consistent with a dense pumice-lapilli layer (Manga et al., 2025; Metcalfe et al., 2025b). Toward Santorini, the internal stratigraphy of Unit CSK1 becomes more difficult to distinguish as the several eruptive units show basal erosion and are internally more chaotic (Figure 2a).

Unit CSK2 comprises oozes with multiple ash layers derived from eruptions ranging from the extrusive to moderately explosive phases of Modern Santorini (~570 ka–250 ka) to Ancient Santorini (Metcalfe et al., 2025a) (Figure 2b). We subdivide it into three subunits CSK2a, CSK2b, and CSK2c. Unit CSK2a includes known Santorini eruptions such as Cape Therma 3 (200 ka) and Cape Therma 1 (230 ± 10 ka), as well as newly discovered Tephras D, E, and H and Tephra Series F, G, I, and J (189–750 ka) (Metcalfe et al., 2025a, 2026) (Figure 2b). Biostratigraphic markers within this interval indicate ages between ~470 and 610 ka. Seismically, this subunit forms well-stratified, laterally continuous, medium-amplitude reflections (Figure 2b). In contrast to the megabeds of CSK1, the laterally continuous, well-stratified reflections of Unit CSK2a reflect a combination of hemipelagic oozes and volcanic fallout deposits, which tend to drape existing topography more uniformly than gravity-driven flows. Unit CSK2b corresponds to the volcanic megabed of the Archaeos eruption (~765 ka; Metcalfe et al., 2025a; Beethe et al., 2025), consisting of lapilli to ash deposits that produce a regionally traceable, chaotic to weakly transparent seismic unit between Horizons csk2a and csk2b (Figure 2b). Unit CSK2c contains Tephra Series K (775–940 ka) and thin to moderately thick volcanic beds (Figure 2b). It is characterized by chaotic to semi-transparent internal reflections similar to those of the Archaeos megabed (Figure 2b). Each subunit is bounded by distinct reflections (Figure 2b). Note that Metcalfe et al. (2025a, 2025b, 2026) incorporated Unit CSK2c into their Unit CSK3; however, our basin-wide assessment indicates that Unit CSK2c exhibits seismostratigraphic characteristics more akin to Unit CSK2b than to Unit CSK3.

Unit CSK3 contains biostratigraphic markers indicating an age range from ~1 Ma to >2 Ma (Druitt et al., 2024b) (Figure 2c). It comprises predominantly oozes with interbedded sands, dolomitic sands, conglomerates, and sandstones (Figure 2c). Seismically, it displays well-stratified, medium-amplitude reflections that locally become chaotic, with abundant internal faulting (Figure 2c). Beneath CSK3 lies the acoustic basement comprising limestones and marbles of Early Pleistocene to Cretaceous age (Figure 2c) (Druitt et al., 2024b).

4.2. Internal Architecture of the Eastern Anhydros and Anafi Basins

The stratigraphy of the eastern Anhydros Basin is constrained by Site U1589 (Druitt et al., 2024c) (Figures 3a and 3b), while that of the eastern Anafi Basin is constrained by Site U1592 (Kutterolf et al., 2024b) (Figures 3b and 3c). Both basins contain major asymmetric grabens that are bound by non-planar normal faults, the East Ios Fault and the Santorini–Anafi Fault (Figures 3a, 3c, and 3d). Unit CSK1 forms a thick basin-fill sequence in both basins (Figures 3a, 3c, and 3d). Internal reflections within this unit correspond largely to volcanic megabeds (Metcalfe et al., 2025a, 2025b). In the Anafi Basin, the Kos Plateau Tuff constitutes the dominant component of the basin fill, forming a major depositional unit that exceeds 200 m in thickness (Metcalfe et al., 2025b). In contrast, volcanic megabeds of Santorini's CFSE activity, including the Minoan, Cape Riva, Lower Pumice 1 and Lower Pumice 2, are thinner in the Anafi Basin than in the Anhydros Basin (Figures 3a, 3c, and 3d). In both basins, most internal reflections of Unit CSK1 onlap toward the basal reflection csk1 (Figures 3a, 3c, and 3d).

Unit CSK2a is well stratified and shows moderate thickening towards the basin-bounding faults. The Archaeos deposit (orange in Figures 3a, 3c, and 3d) is thin at Site U1589 (8 m; Figures 3a and 3b) but becomes substantially thicker in the Anafi Basin, reaching ∼50 m in the seismic profile shown in Figure 3c (Druitt et al., 2024a) and exceeding 100 m in the profile shown in Figure 3d. In both basins, the Archaeos deposit thickens toward the basin-bounding faults (Figures 3a and 3b). The base reflection of Unit CSK2b and the internal reflections of Unit CSK2c onlap the basal reflection csk2c, displaying similar depositional behavior to the reflections observed within Unit CSK1 (Figures 3a, 3c, and 3d).

Unit CSK3 represents a well-stratified succession that thickens toward the East Ios Fault in the Anhydros Basin (Figure 3a), whereas its thickness in the Anafi Basin appears largely unaffected by the Santorini–Anafi Fault (Figures 3c and 3d). In the seismic profile shown in Figure 3c, Unit CSK3 thins toward the central Anafi Basin but thickens towards the northeast. In contrast, the seismic profile in Figure 3d shows Unit CSK3 maintaining an approximately constant thickness across this part of the Anafi Basin.

Both basins exhibit complex internal fault zones. These are most clearly developed in the profile shown in Figure 3d, where faults are synthetic in the northwestern part of the graben but become antithetic toward the southeast, forming localized subsidence zones. In the Anafi Basin, the internal faults dip at approximately 60° (Preine et al., 2020). Most of these faults show a significantly smaller throw within Unit CSK1 compared to the underlying seismostratigraphic units. No internal faults are observed in the Anafi basin in the seismic profile crossing Site U1592 (Figure 3c).

4.3. Internal Architecture of the Western Anhydros Basin

The stratigraphy of the western Anhydros Basin is constrained by Sites U1590 and U1593 (Druitt et al., 2024d; Kutterolf et al., 2024c; Metcalfe et al., 2026), which are located on the hanging wall and footwall of the Kolumbo Fault, respectively (Figures 4a–4d), and supported by seismostratigraphic correlations with Site U1589. Site U1590 lies ∼4.5 km northwest of Kolumbo and was drilled to 627 m below seafloor (mbsf) (Figure 4b). Challenging drilling conditions resulted in limited recovery (∼14%) below 60 mbsf. Site U1593, situated ∼3 km farther northwest on the footwall of the Kolumbo Fault, reached 250 mbsf with a better recovery (∼63%) (Figures 4a and 4b).

Using our revised seismostratigraphic framework, we identify the three major seismostratigraphic units (CSK1–CSK3) in the western Anhydros Basin, which are shown on two representative seismic profiles crossing Kolumbo (Figure 4a) and volcanic centers VC5 and VC6 of the Kolumbo Volcanic Chain (Figure 4c). The Kolumbo Fault stands out as a major tectonic structure, offsetting all seismostratigraphic units (Figures 4a, 4c, and 4d). We measure an offset of the basement reflection of ∼220 m (Figure 4e). This offset remains approximately constant across the unconformities csk2c and csk2a and decreases to ∼140 m at unconformity csk1 (Figure 4e). It is draped by the Minoan and 1650 CE Kolumbo (seismic edifice K5) deposits, making it a blind fault at the surface (Figures 4a and 4c). This substantial displacement has not been recognized in previous studies and caused seismostratigraphic miscorrelations between the volcano-sedimentary strata in the hanging wall and footwall of the Kolumbo Fault (Crutchley et al., 2023; Hübscher et al., 2015; Nomikou et al., 2016; Preine, Hübscher, et al., 2022; Preine, Karstens, Hübscher, Nomikou, et al., 2022; Preine, Karstens, Hübscher, Crutchley, et al., 2022). A depth-converted seismic image shows the Kolumbo Fault as having a non-planar, listric geometry, dipping ∼60° near the surface and progressively flattening to ∼35° toward the acoustic basement (Figures 4a, 4c, and 4e).

10.1029/2025GC012897

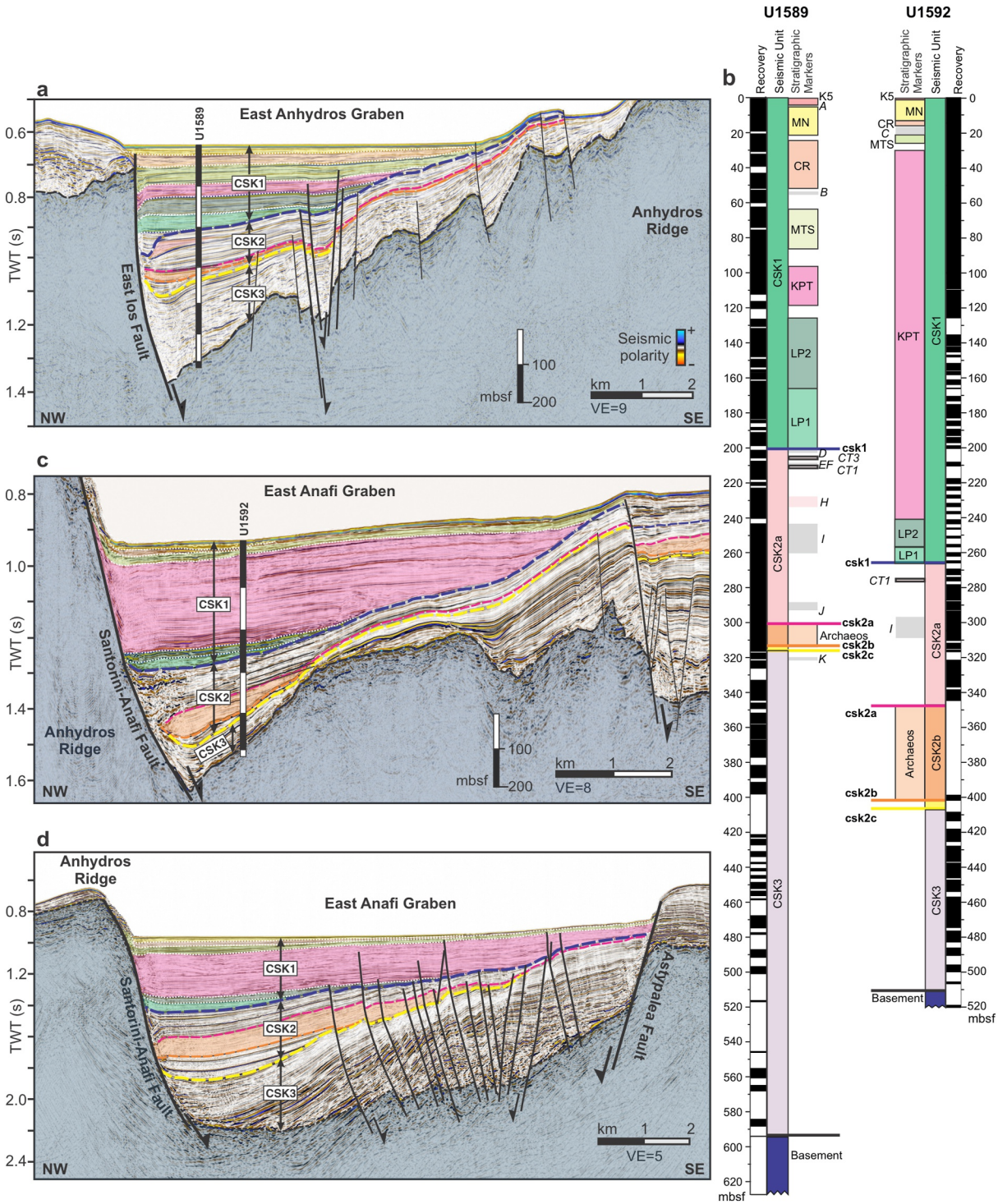

Figure 3. Core-seismic integration at the eastern Anhydros and Anafi Basins. (a) Seismic profile crossing the eastern Anhydros Basin with Site U1589. Core-seismic integration after Preine et al. (2025). Black and white bars indicate depth intervals of 100 m at the drill site. Semi-transparent blue color indicates acoustic basement; orange: Archaeos (Druitt et al., 2024a); other: volcanic eruptions from Santorini and Kos after Metcalfe et al. (2025a, 2025b) as detailed in (b). (b) Recovery (black), depths of seismostratigraphic units, and volcanic markers at Sites U1589 and U1592. MN: Minoan (3.6 ka); CR: Cape Riva (22 ka); MTS: Middle Tuff Sequence (177–22 ka); KPT: Kos Plateau Tuff (161 ka); LP2: Lower Pumice 2 (177 ka); LP1: Lower Pumice 1 (186 ka). Gray boxes indicate Tephra layers and series A-K as detailed in Figure 1d. mbsf: meters below seafloor. (c) Seismic profile crossing the eastern Anafi Basin with Site U1592. Colors as in (a). (d) Seismic profile crossing the eastern Anafi Basin with stratigraphy projected from Site U1592 through seismostratigraphic correlation. Colors as in (a). The location of the seismic profiles are shown in Figure 1b. Non-interpreted versions of the seismic profiles are provided in Figure S2 in Supporting Information S1. TWT: Two-Way Travel time of seismic waves. VE = Vertical Exaggeration.

Using our dense grid of seismic lines, we trace the Kolumbo Fault laterally for at least 23 km, with a general NE–SW strike of 017°–060°, subparallel to the Kolumbo Volcanic Chain and to the regional tectonic trend of the SATZ (Figures 1b and 1c). The fault is distinct from the West Ios Fault (Figure 4c) and forms the marginal boundary of an asymmetric graben bounded to the southeast by the Anhydros Ridge (Figures 4a and 4c). This whole structure is hereafter referred to as the *Kolumbo Graben*. Kolumbo Volcano and its associated Kolumbo Volcanic Chain edifices are situated near the center of the Kolumbo Graben, approximately 4.5–8 km from the Kolumbo Fault (Figures 4a and 4c).

Outside the Kolumbo Graben, on the footwall of the Kolumbo Fault, individual eruptive units are difficult to distinguish and Unit CSK1 is thin (~60 m at Site U1593) (Figures 4a–4e). On the hanging wall of the Kolumbo Fault, Unit CSK1 is much thicker (~260 m at Site U1590) and major eruptive units from Kolumbo and Santorini can be traced as volcanic megabeds, as also observed in the western Anafi and Anhydros Basins (Figures 3 and 4a–4e). In the Kolumbo Graben, the Santorini megabeds are interbedded with eruptive units of Kolumbo and the Kolumbo Volcanic Chain (Figures 4a–4e). Our seismic images, groundtruthed by deep-drilling (Metcalfe et al., 2026), show that Kolumbo's Unit K1/K2 lies beneath the Lower Pumice 1 eruption (186 ka), the K4 tephra overlies the Middle Tuff Sequence, while K5 marks the uppermost Kolumbo unit above the Minoan deposits (Figures 4a, 4b, and 4d). The flanks of Kolumbo Volcanic Chain cone VC5 pinch out within the Middle Tuff Sequence (Figure 4c). These stratigraphic relationships are consistent with the eruptive chronology established by Metcalfe et al. (2026) and Vougioukalakis et al. (2025), which places the earliest Kolumbo eruptions (K1/K2) between 265 and 193 ka, and K4 at ~24 ka (Metcalfe et al., 2026). VC5 appears to have been formed at a similar time as VC15 (~34 ka; Vougioukalakis et al., 2025) (Figures 1c and 1d), consistent with its position above the Middle Tuff Sequence (177–22 ka).

Numerous smaller syn- and antithetic faults are present within the Kolumbo Graben (Figures 1b, 4a, and 4c). Beneath Kolumbo and the Kolumbo Volcanic Chain, acoustic blanking obscures internal structures, yet the similar dip angles and depths of seismic horizons on both sides of the volcanic edifices suggest that no major fault is located directly beneath them (Figures 4a and 4c). Toward Santorini, we observe one smaller volcanic cone that lies on top of the Kolumbo Fault (Figure 4f). The flanks of this edifice are intercalated within Unit CSK1 but distinctly offset, lying 40–50 m deeper on the hanging-wall of the Kolumbo Fault compared to the footwall (Figure 4f).

4.4. Horizon-Flattening Across the Kolumbo Fault

In order to relate the vertical displacement along the Kolumbo Fault plane to the dated stratigraphic markers, we applied horizon-flattening to a depth-converted profile across the Kolumbo Fault (Figures 5a–5e), the only major fault where reliable footwall–hanging-wall correlations are possible. Although flattening implicitly implies the likely incorrect assumption of a flat seafloor at each horizon, it remains a proxy for relative thickness changes and relative changes in accommodation space.

We flattened four key horizons: unconformity csk1 (186 ka), the base of Unit K1/K2 (~265 ka), and unconformities csk2a (~765 ka) and csk2c (~1 Ma). Without flattening, the base of CSK1 shows ~140 m of offset and a more than fourfold thickening on the hanging wall (Figure 5a). After flattening CSK1, underlying units show only ~60 m of throw (Figure 5b). Flattening the base of K1/K2 further reduces apparent displacement, with Unit CSK2a showing only ~20 m of throw and a factor of ~1.6 thickening (Figure 5c). After flattening Horizon csk2a, nearly all observable offset disappears, and internal reflections in Unit CSK3 dip gently SE with no discernible separation (Figures 5d and 5e). Thus, we observe no significant thickness differences along the Kolumbo Fault in Subunits CSK2b and CSK2c, as well as Unit CSK3 (Figures 5d and 5e).

These relationships indicate that the Kolumbo Fault initiated after ~765 ka, following deposition of Subunit CSK2b (Archaeos eruption), which shows no fault-related thickening, corroborated by adjacent profiles (Figure S4 in Supporting Information S1). Given that the Archaeos Tuff is a volcanic megabed (Druitt et al., 2024a) which was emplaced almost instantaneously on a geological timescale as a density current, it formed a bathymetry-filling deposit with an essentially flat surface after deposition (Druitt et al., 2024a; Metcalfe et al., 2025a). Such beds therefore preserve the pre-existing substrate dip and provide an accurate record of true tectonic subsidence.

After the deposition of the Archaeos, our horizon-flattening results suggest subtle movement along the Kolumbo Fault between ~765 and ~250 ka. A pronounced increase in subsidence must have occurred before 186 ka,

10.1029/2025GC012897

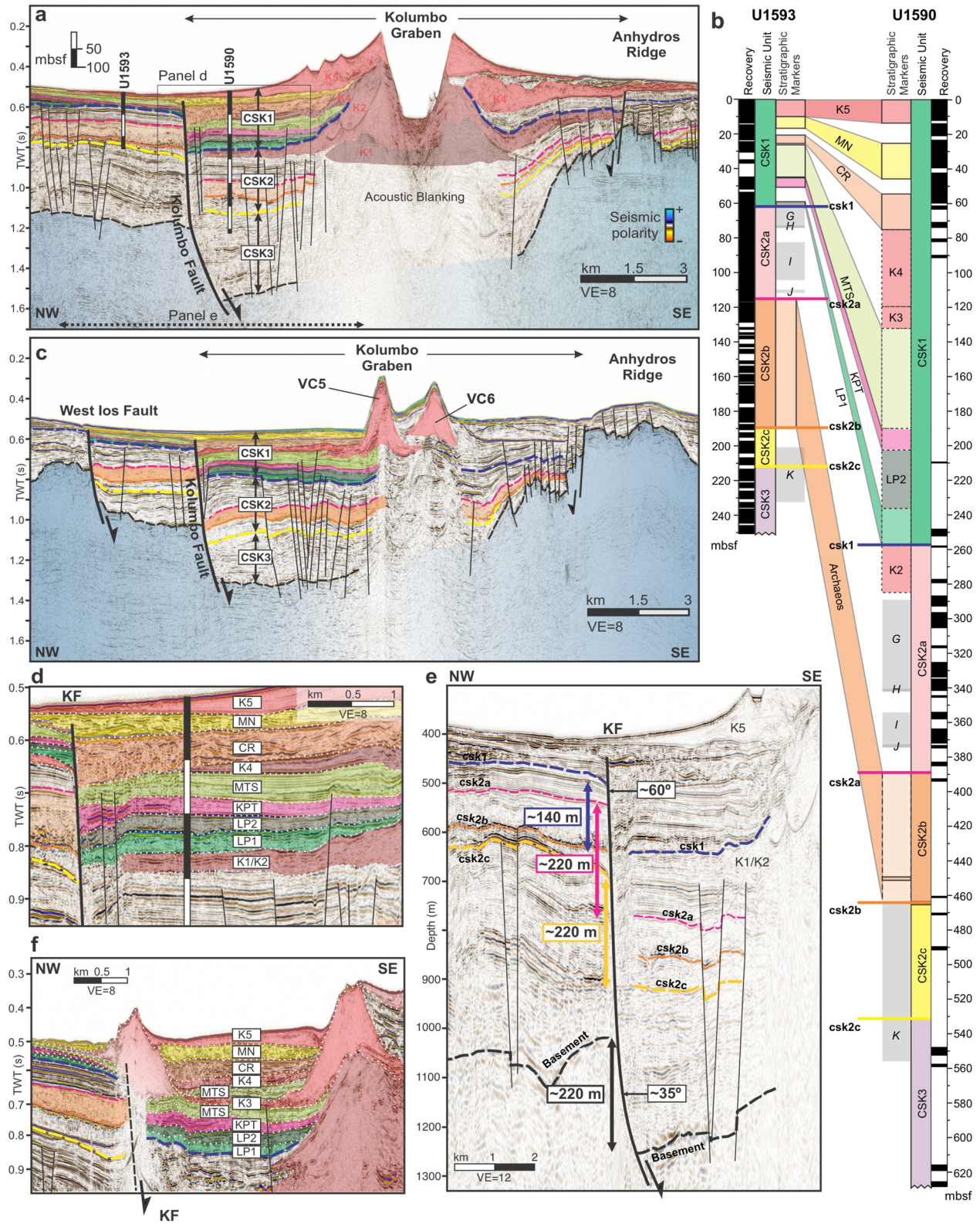

Figure 4.

creating accommodation space for the thick volcanic megabeds sourced from Santorini and eruptive deposits from Kolumbo. Subsidence continued as the Kolumbo Fault cuts through all subsequently emplaced volcanic units except for the deposits of Kolumbo's last eruption K5 (Figure 4d).

4.5. Basin Architecture

Using our dense grid of seismic profiles (Figure S1 in Supporting Information S1), we present maps of the seafloor reflection, the basal reflections of the main seismostratigraphic units (Horizons csk1, csk2 and csk3), as well as corresponding isochore maps of the total sedimentary thickness and of the main Units CSK1-CSK3 (Figure 6), which we convert into isochrone maps using average P-wave velocities measured during IODP Expedition 398 (Figure 2).

Mapping the seafloor reflection, we derive a map similar to the multibeam-derived seafloor, highlighting the resolution of the combined seismic grid, constrained by ∼160 multichannel seismic profiles (Figure 6a). Both the Anafi and Anhydros Basins are visible as broad NE-SW striking depressions, separated by the Anhydros Ridge (Figure 6a). The distribution of the total sedimentary cover reveals a more complex depositional system, with major depocenters in the eastern Anafi Basin (maximum sediment thickness ≤1,300 m), followed by an accumulation at the western Anhydros Basin (≤1,100 m), the western Anafi Basin (≤750 m), and the eastern Anhydros Basin (≤700 m) (Figure 6b).

Mapping of the base of Units CSK1-3 indicates a segmentation of the major basins into several depression, with individual depressions being more or less active through time. Informed by our seismic profiles, we refer to these depressions in the following as separate tectonic graben structures: East Anafi Graben, West Anafi Graben, East Anhydros Graben, Kolumbo Graben, and West Anhydros Graben (Figure 6c).

Mapping of the base of Unit CSK1 (i.e., unconformity csk1) indicates three major structural depressions: the East Anafi Graben, the East Anhydros Graben and in the Kolumbo Graben (Figure 6c). The Kolumbo Graben marks a structural depression defined by a sharp boundary to the west, corresponding to the Kolumbo Fault, and a topographical high in the east, corresponding to the Anhydros Ridge that connects SE Santorini to Anhydros island (Figure 6c). The Kolumbo Graben is bound to the NE by a topographical high, marking a separation towards the East Anhydros Graben, which forms a broadly ENE–WSW-oriented depression (Figure 6c). Reflection csk1 lies at a similar depth in both the East Anhydros Graben and in the Kolumbo Graben (Figure 6c). The East Anafi Graben marks the deepest and most prominent structural depression of reflection csk1 (Figure 6c). The thickness distribution of Unit CSK1 shows strong lateral variations (Figure 6d). The greatest sediment accumulation of Unit CSK1 lies in the East Anafi Graben (≤400 m), followed by the Kolumbo Graben (≤320 m), with the thickness accumulation strongly controlled by the Kolumbo Fault (Figure 6d). Sediments of Unit CSK1 in the East Anhydros Graben reach a maximum of ≤230 m and sediment accumulation is clearly separated from that of the Kolumbo Graben by the previously described topographical high NW of Anhydros (Figure 6d).

The base of Unit CSK2 (i.e., unconformity csk2) further highlights the pronounced segmentation of the basins (Figure 6e). The most prominent depression corresponds to the East Anafi Graben, with a continuation to the western Anafi Basin. In the western Anhydros Basin, we image a broader depression that is not restricted to the Kolumbo Fault but extends farther westward (Figure 6e). To the east, this depression is bound by the

Figure 4. Core-seismic integration across the Kolumbo Fault. (a) Seismic profile crossing the Kolumbo Fault and Kolumbo with Sites U1590 and U1593. Black and white bars indicate depth intervals of 100 m at the drill site. Core-seismic integration after Preine et al. (2025). Semi-transparent blue color indicates acoustic basement; orange: Archaeos (Druitt et al., 2024a, 2024b, 2024c, 2024d, 2024e; Metcalfe et al., 2026); red: Kolumbo Eruptions (K1-K5); other: volcanic eruptions from Santorini and Kos as detailed in (b) (Metcalfe et al., 2026). (b) Recovery, depths of seismostratigraphic units, and volcanic markers at Sites U1590 and U1593 based on Metcalfe et al. (2026) and Druitt et al. (2024a). MN: Late Bronze Age (3.6 ka); CR: Cape Riva (22 ka); MTS: Middle Tuff Sequence (177–22 ka); KPT: Kos Plateau Tuff (161 ka); LP2: Lower Pumice 2 (177 ka); LP1: Lower Pumice 1 (186 ka). Dashed boxes indicate volcanic units that were not directly recovered but inferred from seismostratigraphic correlations. Gray boxes indicate Tephra layers and series A-K as detailed in Figure 1d. mbsf: meters below seafloor. (c) Seismic profile crossing the Kolumbo Fault and the Kolumbo Volcanic Chain. Colors as in (a) but red colors indicate Kolumbo Cones. (d) Zoom of the uppermost volcano-sedimentary strata west of Kolumbo from seismic profiles in (a) with interpreted volcanic units highlighted after Metcalfe et al. (2026). Locations are indicated by the rectangle in (a). (e) Depth-converted seismic profile across the Kolumbo Fault. The lateral extent of the excerpt is shown in panel (a) by the horizontal dotted lines. Dashed colored lines mark major seismostratigraphic units and correlated conformities. Bold numbers denote the throw of major unconformities measured along the Kolumbo Fault and the measured dip angles of the Kolumbo Fault. (f) Seismic profile crossing an isolated volcanic cone (VC) northeast of Santorini. Colors as in (a) (KF: Kolumbo Fault. For location of all seismic profiles, see Figure 1b. Non-interpreted versions of the seismic profiles are provided in Figure S3 in Supporting Information S1. TWT: Two-Wav Travel time of seismic waves. VE = vertical exaggeration.

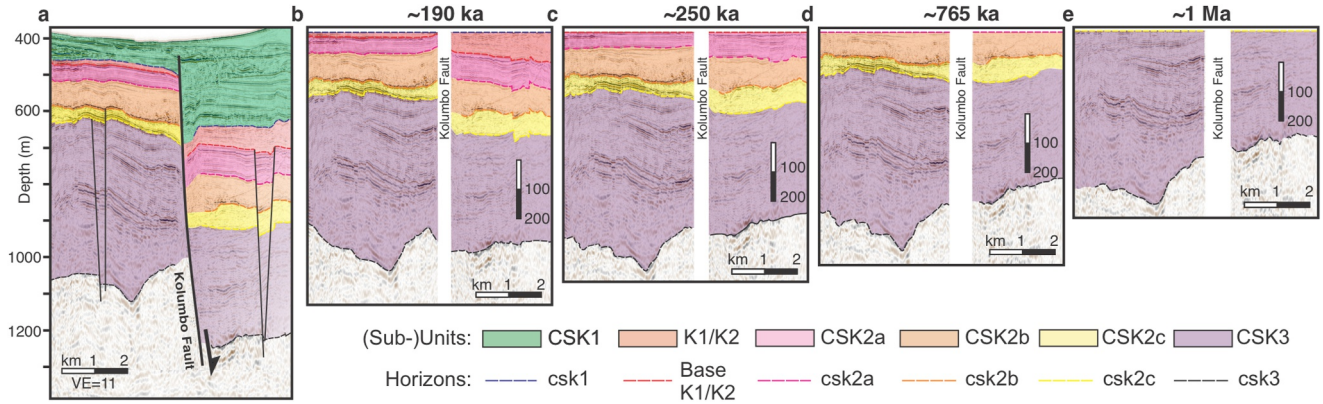

Figure 5. Horizon-flattening of a depth-converted seismic profile crossing the Kolumbo Fault. (a) Unflattened profile. (b) Profile flattened to Horizon csk1 (~190 ka). (c) Profile flattened to the base of K1/K2 (~250 ka). (d) Profile flattened to Horizon csk2a (~765 ka). (e) Profile flattened to Horizon csk2c (~1 Ma). Semi-transparent colors denote the main seismostratigraphic units.

Santorini–Anhydros Ridge, which forms a well-defined topographic high. We refer to this depression as the West Anhydros Graben, with the Kolumbo Graben representing a subset of this broader structure (Figure 6e). To the NE, we image a clear topographical rise, separating the West and East Anhydros Grabens. The thickness distribution of Unit CSK2 reflects this structural pattern: the eastern Anhydros Basin hosts only minor sediment accumulation (≤140 m), whereas the western Anhydros Basin is a major depocenter (≤220 m), which broadly infills the West Anhydros Graben and is not confined to the Kolumbo Fault (Figure 6f). The main depocenter of Unit CSK2 is the East Anafi Graben (≤360 m), separated from a broad depocenter within the western Anafi Basin (≤220 m) (Figure 6f).

The base of Unit CSK3 (i.e., unconformity csk3) further underscores the structural segmentation of the basin (Figure 6g). The Anhydros Basin is segmented by a prominent basement rise, striking roughly NNW-SSE. The most pronounced depression is again the East Anafi Graben, separated by another distinct depression in the West Anafi Graben (Figure 6g). The Anhydros Basin is clearly separated into the East and West Anhydros Grabens, with the West Anhydros Graben forming a broad depression, not limited to the Kolumbo Graben. The Anhydros Ridge is imaged as a distinct, narrow structural high, connecting Anhydros island with the SE of Santorini, where Alpine Basement is exposed (Figure 6g) (Druitt et al., 1999). The thickness distribution of Unit CSK3 indicates broad accumulations that do not follow the general NE-SW trend of the graben structures and seem to be not strictly controlled by topographical depressions (Figures 6g and 6h). In the eastern Anhydros Basin, deposits partly extend across the Anhydros Ridge along a roughly NNW–SSE-trending corridor that connects to the eastern Anafi Basin (Figure 6g). In the West Anhydros Graben, thick accumulations (≤670 m) occur toward the southeast of Ios Island. The eastern Anafi Basin exhibits a broad depocenter that is oriented roughly WSW–ENE and includes smaller, enclosed depocenters reaching a maximum thickness of >700 m. In the western Anafi Basin, Unit CSK3 thickens around the northwestern flank of Anafi (≤730 m) and toward the Anhydros Ridge (≤600 m) (Figure 6g).

4.6. Temporal Evolution of Basin Subsidence and Extension

To quantify the temporal evolution of subsidence, we reconstruct basin-scale subsidence in the non-volcanic rift basins using a geometric rotation approach (Figure 7). Volcanic megabeds are treated as near-instantaneously-emplaced, bathymetry-filling deposits with surfaces that were originally horizontal (Figures 7a–7d). In contrast, intervening non-volcanic strata may have accumulated on inclined surfaces in a starved rift setting and therefore are considered to not provide reliable paleo-horizontal reference levels (Figures 7a–7d). Following emplacement, progressive basin subsidence induced tilting of the megabed surfaces, such that their present-day dip angles record cumulative post-depositional tilting.

For each seismic profile, a measurement point was established 2–3 km from the main bounding fault to minimize boundary effects, such as localized fault drag or the presence of coarse talus and detritus (Figure 7e). A structural

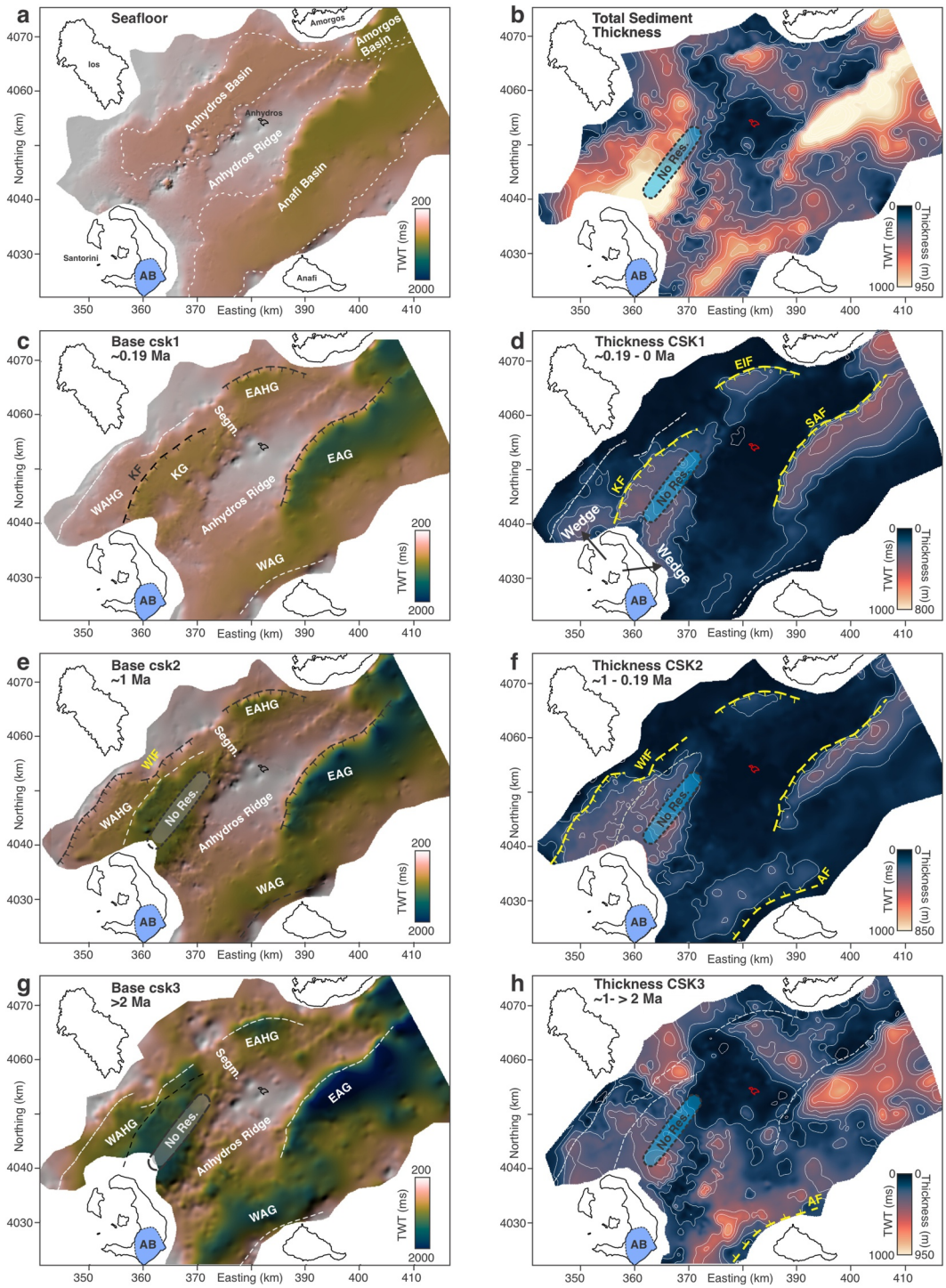

Figure 6.

hinge point was then determined by extrapolating the non-volcanic reference Horizons csk1 and csk2c; the hinge corresponds to their point of intersection (Figures 7e–7h). Dip angles (α) of individual megabed tops were measured at the fixed reference location. To account for manual picking uncertainties, we assigned a constant error of ±0.1° to all bed dip measurements. Vertical subsidence (Z) was calculated by treating the distance between hinge and measurement point as a lever arm (L), such that $Z = L \cdot \tan(\alpha)$. Uncertainties in Z were propagated from the dip error using the derivative of the tangent function ($L \cdot \sec^2(\alpha) \cdot \Delta\alpha$). Time-averaged subsidence rates were obtained from the incremental subsidence between successive markers (ΔZ) divided by the corresponding age difference (Δt). Horizontal extension rates (E) were subsequently estimated using the geometric relationship $E = \Delta Z/\tan(\beta)$, where β represents the specific dip angle of the main bounding fault for each profile (Figure 7e). Total uncertainties for both subsidence and extension rates were calculated using Gaussian error propagation, incorporating the cumulative picking errors and an assumed ±5° uncertainty for the fault dip angles.

Across all seismic profiles (East Anafi Graben: HH06-P11, HH06-P14, HH06-P15; East Anhydros Graben: HH06-P15), megabed dip angles decrease systematically up-section (Figures 7f–7i). The oldest marker, the Archaeos megabed (~765 ka), exhibits the steepest tilts, reaching ~4° in the East Anafi Graben and ~1° in the East Anhydros Basin, whereas the Lower Pumice 1 megabeds shows significantly smaller dip angles in the order of ~1.4° in the East Anafi Graben and ~0.45° in the East Anhydros Basin (Figure 7i). Most of the total subsidence is measured in the time between the Archaeos and Lower Pumice I eruption, with the East Anafi Graben recording a subsidence of ~185–340 m and the East Anhydros Graben ~85 m (Figure 7j). Tilt angles and estimated subsidence show a sharp decline between the Lower Pumice I and Kos Plateau Tuff megabeds, with both values decreasing to nearly half (Figures 7i and 7j).

While calculated subsidence rates during the early phase (Archaeos to LP I; ~765–186 ka) are modest and relatively steady, it is important to note that the absence of additional data points precludes us from resolving potential variations in this ~600 kyr interval (Figures 7k and 7l). In the East Anafi Graben, subsidence rates range from ~0.3 to 0.6 m kyr^{-1}, with estimated extension rates being in the order of ~0.4–0.7 m kyr^{-1}. In the East Anhydros Basin, we estimate a subsidence rate of ~0.1 m kyr^{-1} and an extension rate of ~0.15 m kyr^{-1} in the interval between the Archaeos and LP I eruption. A pronounced, basin-wide acceleration in subsidence and extension is observed between LP I and LP II (~188–177 ka) (Figures 7k and 7l). During this interval, estimated subsidence rates increase to ~2–5 m kyr^{-1} and extension rates to ~3–4.5 m kyr^{-1}, representing a four- to eightfold increase relative to the preceding background phase. In the East Anhydros Basin, subsidence rates rise to ~0.7 m kyr^{-1} and extension rates to ~0.66 m kyr^{-1}, corresponding to approximate increases by factors of 3–5 (Figures 7k and 7l). While the actual changes in dip angle and subsidence between these horizons may appear subtle (Figures 7i and 7j), the short duration of this interval (~11 kyr) translates even minor angular differences into significantly higher subsidence rates compared to the long-term background (Figures 7k and 7l).

Elevated deformation persists until the emplacement of the Kos Plateau Tuff, with subsidence rates of ~3.6 m kyr^{-1} and extension rates of ~2.9 m kyr^{-1} in the East Anafi Basin (Figures 7k and 7l). Thereafter, subsidence and extension rates decline markedly by a factor of ~6–10 between the Kos Plateau Tuff and Cape Riva intervals. A secondary increase of subsidence rates is recorded between the Cape Riva and Minoan eruptions, followed by a final decrease towards present-day values of ~0.3–0.9 m kyr^{-1}, which translates to extension rates of ~0.5–1.5 m kyr^{-1} (Figures 7k and 7l).

Figure 6. Gridded seismostratigraphic horizons and derived thickness maps. Gridded surfaces of the main seismostratigraphic horizons (left panels) alongside their corresponding isochrone and approximated isochore maps (right panels) picked form seismic profiles. (a) Seafloor picked from seismic profiles. Dashed lines indicate basin structures after Nomikou et al. (2018). (b) Total thickness of sediments (*basement minus seafloor reflection*). Thin white lines indicate 100 ms contour lines. (c) Gridded map of Horizon csk1 with hillshade. Segm.: Segmentation of the Anhydros Basin. KF: Kolumbo Fault; KG: Kolumbo Graben; EAG: East Anafi Graben; WAG: West Anafi Graben; EAHG: East Anhydros Graben; WAHG: West Anhydros Graben. Black faults are inferred to be active faults in the depicted time interval; white faults are inferred to be inactive. (d) Thickness map of Unit CSK1 (=*csk1 minus seafloor*). Encompasses the volcanic megabeds from Thera Pyroclastic Formation and the Kos Plateau Tuff eruption (Metcalfe et al., 2025a, 2025b), as well as the eruptions of Kolumbo edifices K3-K5 (Metcalfe et al., 2026). EIF: East Ios Fault; KF: Kolumbo Fault; SAF: Santorini-Anafi Fault. (e) Gridded map of Horizon csk2c with hillshade. (f) Thickness map of Unit CSK2 (=*csk2c minus csk1*). Encompasses Kolumbo's eruptions K1 and K2, as well as the Archaeos (Druitt et al., 2024a). WIF: West Ios Fault. AF: Anafi Fault. (g) Gridded map of Horizon csk3 (basement reflection) with hillshade. (h) Thickness map of Unit CSK3 (=*basement reflection minus csk2c*). Gray and blue semi-transparent area indicates region with no resolution due to acoustic blanking underneath the Kolumbo Volcanic Chain. AB: Alpine Basement onshore Santorini, shown to highlight asymmetric outcrop on Santorini (Druitt et al., 1999). Basement outcrops on other islands are not shown. Non-interpreted version of the figure is provided in Figure S5 in Supporting Information S1. A map showing all seismic profiles used for the mapping is provided in Figure S1 in Supporting Information S1.

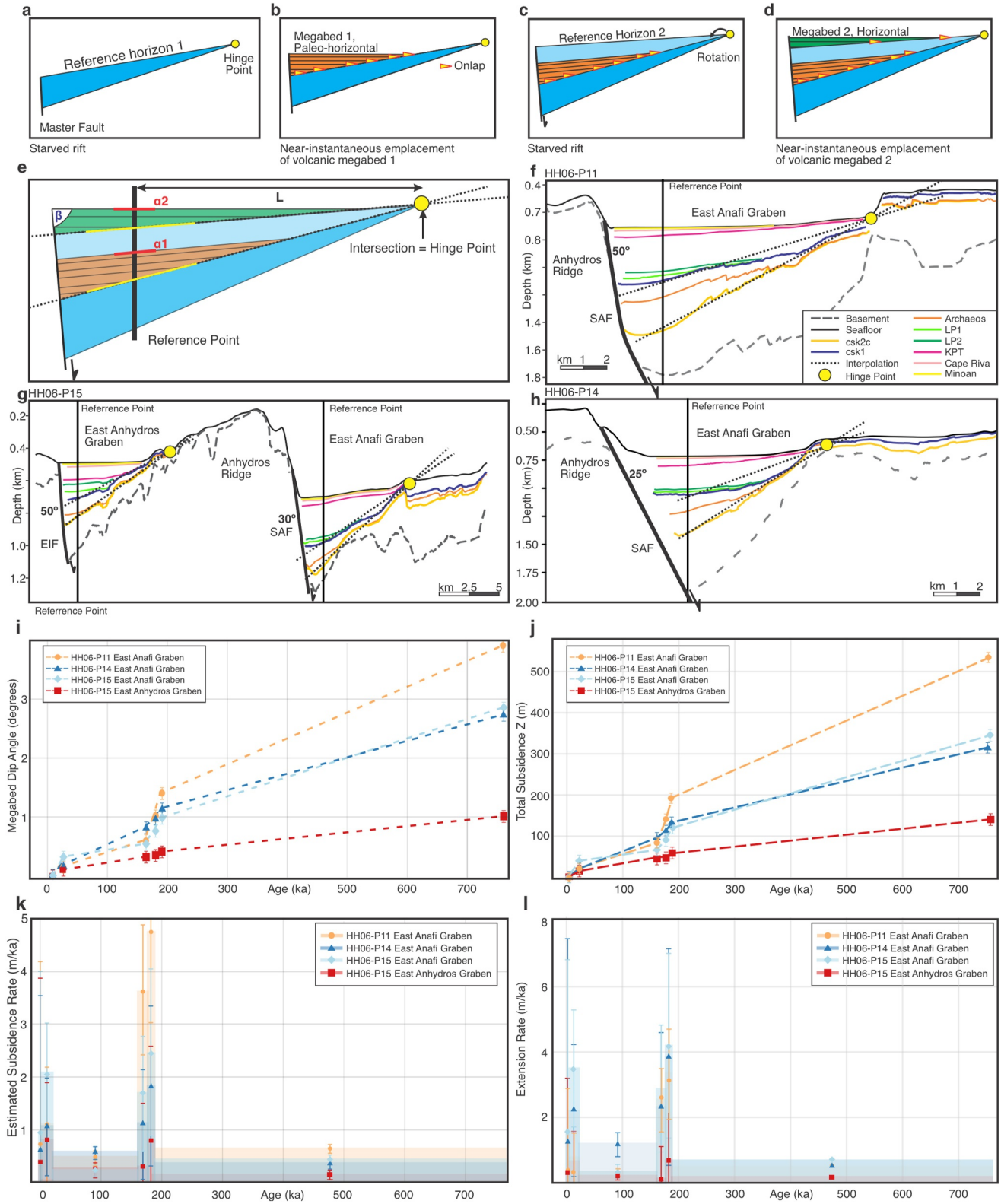

Figure 7.

4.7. Cumulative Offset Histories of Faults

To assess the evolution of individual faults, we measured vertical separation (throw) at a series of offset–age pairs on four faults where both hanging-wall and footwall stratigraphic geometries are accessible: (a) the Kolumbo Fault (Figures 8a, 8e, and 8i), (b) an internal fault within the broader West Anhydros Graben (Figures 8b, 8f, and 8j), (c) an intra-basinal fault in the East Anhydros Graben (Figures 8c, 8g, and 8k), and (d) an intra-basinal fault in the East Anafi Graben (Figures 8d, 8h, and 8l). These locations allow reliable core-seismic integration using chronostratigraphic markers drilled at IODP Expedition 398 sites (U1589, U1590, U1592, U1593; Figure 1b). Tie points include well-constrained volcanic megabeds: Archaeos (765 ka), Lower Pumice 1 (186 ka), Lower Pumice 2 (177 ka), Cape Riva (22 ka), Minoan (3.6 ka), Cape Therma 1 (~230 ka), K1/K2 (~265–193 ka; simplified to ~250 ka), K4 (~24 ka), plus tephra layers H (~330 ka) and tephra series J (~645–750 ka).

Estimated cumulative fault throws (blue lines) are shown in Figures 8e–8h. The plots in Figures 8i–8l show estimated time-averaged throw rates between measured fault throw pairs (blue bars) and thickness differences for each volcanic megabed (red bars) calculated by subtracting thicknesses in the hanging-wall from thicknesses the footwall (Supplementary Tables S2-S5).

All four faults exhibit a generally coherent pattern of late Quaternary rift evolution (Figures 8a–8l), implying they respond to similar regional adjustments in the stress regime. The Kolumbo Fault accommodated by far the greatest displacement (~220 m), while the intra-basinal faults in the West Anhydros (~45 m), East Anhydros (~30 m), and East Anafi (~29 m) Grabens recorded significantly lower cumulative throw (Figures 8a–8l).

Between 765 and 330 ka, all structures exhibited modest background activity, with fault throw rates of ~0.1 m kyr^{-1} at the Kolumbo Fault and approximately 0.01 m kyr^{-1} on the other faults (Figures 8e–8l). A marked regional acceleration occurred between 330 and ~186 ka. At the Kolumbo Fault, throw rates rose to ~0.9 m kyr^{-1} (Tephra H to K1/K2), representing an 8-fold increase over the previous interval. During the subsequent Lower Pumice 1–Lower Pumice 2 interval (186–177 ka) we estimate throw rates up to ~3.8 m kyr^{-1}, a further 4-fold acceleration (Figure 8i). Similar trends can be observed in the intra-basin faults: Throw rate estimates in the West Anhydros Graben indicate values of up to ~0.3 m kyr^{-1} (Figure 8j). Throw rates in the East Anhydros and East Anafi Grabens reach ~0.5 and ~0.4 m kyr^{-1}, respectively, reflecting accelerations by factors of >15 compared to the pre-330 ka phase (Figures 8k and 8l).

Following the deposition of the Kos Plateau Tuff megabed (161 ka), much of the earlier displacement was compensated and throw rate estimates decreased significantly across all studied faults, returning to values near the pre-acceleration background (~0.01 m $kyr^{-1}$for intra-basin faults). Another surge in throw rates is measured at the Kolumbo Fault and in the West Anhydros Graben between 26 and 22 ka reaching ~4 m kyr^{-1} and between the 22 and 4 ka (~2.5 m kyr^{-1}), while the internal fault in the West Anhydros Basin rises from ~0.01 m kyr^{-1} to about 0.35 m kyr^{-1} in that interval (Figure 6i).

5. Discussion

5.1. Tectonic Evolution of the Santorini-Amorgos Tectonic Zone

Deciphering the volcano–tectonic evolution of the SATZ is challenging because the stratigraphic record reflects the superposition of two distinct processes: (a) tectonic extension, potentially occurring in temporally variable phases (Metcalfe et al., 2025a; Preine, Hübscher, et al., 2022), and (b) the rapid, episodic infilling of

Figure 7. Temporal evolution of basin subsidence. (a–d) Conceptual illustration of the method to assess the basin subsidence histories. Volcanic megabeds are treated as near-instantaneously-emplaced, bathymetry-filling marker horizons with originally horizontal surfaces, deposited between intervals of background pelagic and syn-tectonic sedimentation in a progressively rotating hanging-wall block. These horizons provide chronostratigraphic markers to reconstruct basin tilting and subsidence. (e) Schematic of the reconstruction approach. For each seismic profile, a hinge point is defined by the intersection of non-volcanic reference horizons. At a fixed measurement point, the dip angles (α_1, α_2) of the tops of successive megabeds are determined. Subsidence between two time intervals is then estimated from the change in dip angle and the distance to the hinge point (L), assuming rigid block rotation. (f–h) Key depth-converted stratigraphic horizons extracted from representative seismic profiles across the East Anafi and East Anhydros grabens. For each volcanic megabed, only the top reflection is indicated and used as a paleo-horizontal reference surface; dashed gray lines indicate basement and seafloor. Yellow circles denote calculated hinge points used for reconstruction. LP1: Lower Pumice 1 (177 ka); LP2: Lower Pumice 2 (186 ka); KPT: Kos Plateau Tuff (161 ka). SAF: Santorini-Anafi Fault; EIF: East Ios Fault. (i) Temporal evolution of megabed dip angles and (j) total subsidence derived from megabed rotation approach. (k) Calculated subsidence rates and (l) estimated extension rates plotted at interval midpoints. A table summarizing all values is provided as Table S1 in Supporting Information S1.

10.1029/2025GC012897

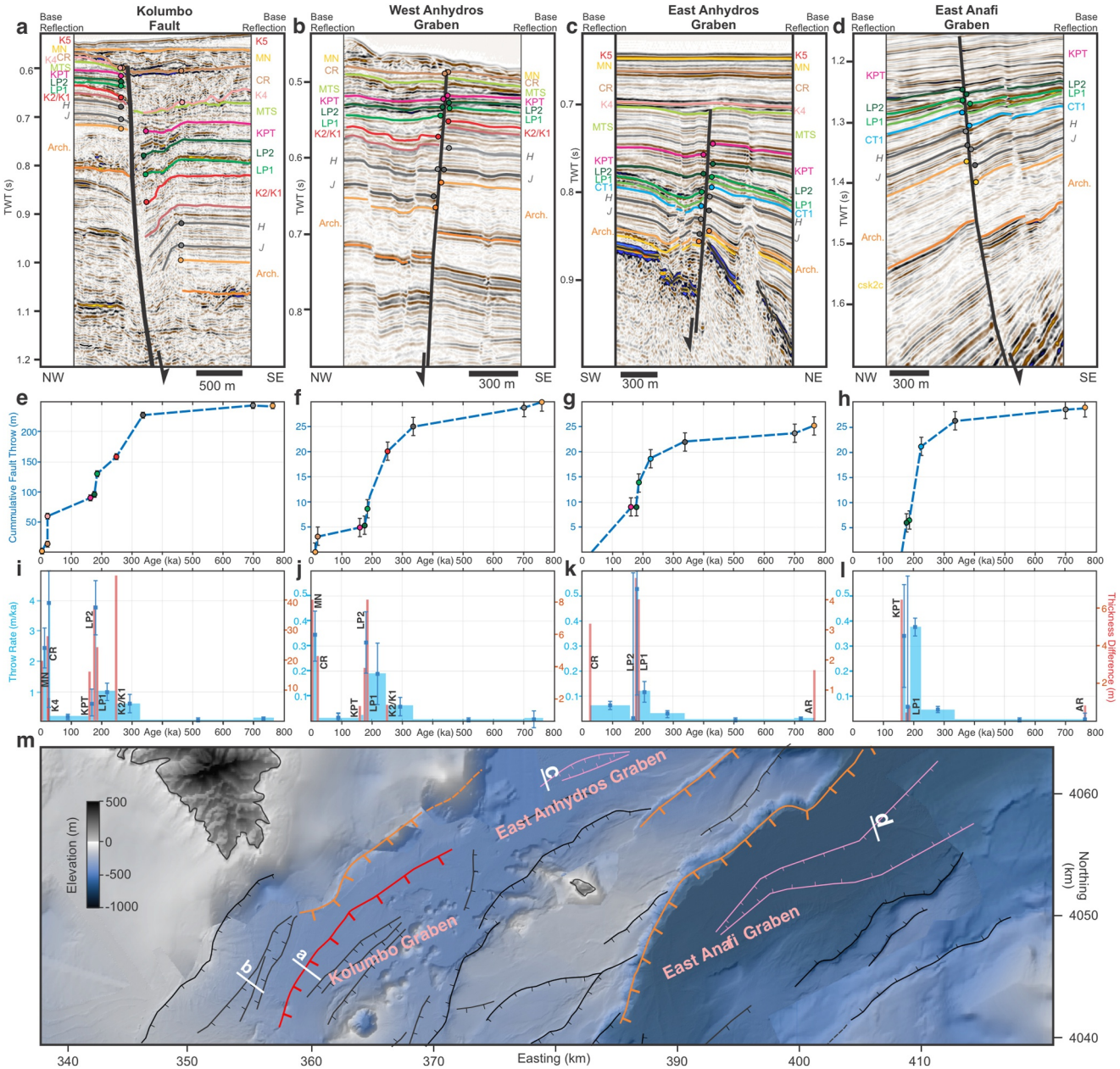

Figure 8. Temporal evolution and fault activity. (a–d) Seismic profiles across major and internal faults in the Santorini-Amorgos Tectonic Zone: (a) Kolumbo Fault, (b) West Anhydros Graben, (c) East Anhydros Graben, and (d) East Anafi Graben. Colored horizons mark chronostratigraphic markers used for offset measurements; circles indicate tie points where throw was quantified. K5: Kolumbo Unit 5 (1650 CE); MN: Minoan (3.6 ka); CR: Cape Riva (22 ka); K4: Kolumbo Unit 4 (~24 ka); MTS: Middle Tuff Sequence (177–22 ka); LP2: Lower Pumice 2 (177 ka); LP1: Lower Pumice 1 (186 ka). K1/K2: Kolumbo Units 1 and 2 (~265–193 ka). (e–h) Temporal development of cumulative fault throw (blue curves) for the four faults shown in (a–d). Tables summarizing all values are provided as Tables S2–S5 in Supporting Information S1. (i–l) Comparison of fault activity and volcanic infill. Blue bars represent estimated incremental throw rates for the four faults shown in (a–d). Red bars depict the thickness difference of volcanic megabeds between the hanging wall and footwall of each fault. (m) Morphological map showing the locations of profiles in panels (a–d); fault colors correspond to Figure 1b.

accommodation space by volcanic megabeds (Metcalfe et al., 2025a, 2025b, 2026). To disentangle these processes, we combine four independent approaches: (a) horizon flattening, (b) thickness mapping of seismic units, (c) rotation-based reconstruction of megabed geometries, and (d) fault throw rate analysis.

Each of these methods is subject to significant uncertainties. Horizon flattening assumes originally horizontal deposition (Figure S6 in Supporting Information S1), which may not hold in starved rift settings (Figure 5).

Thickness variations reflect both tectonic accommodation and volcanic input (Figure 6). Our rotation-based subsidence and extension calculation approach is only constrained by a few volcanic megabeds and is sensitive to uncertainties in dip angles, short time intervals, and hinge-point geometry (Figure 7). Throw-rate estimates derived from cumulative offsets may be biased by preferential thickening of volcanic deposits in the hanging wall (Figure 8). Additional uncertainties arise from uncorrected compaction effects. Shipboard measurements from IODP Expedition 398 show that calcareous oozes experience a porosity reduction of ∼10% within the upper 300 m (Manga et al., 2025), consistent with global compaction trends (Svadlenak et al., 2026). These imply ∼15%–20% total compaction for a 1,000 m thick sequence of pure pelagic ooze. However, Units CSK1 and CSK2 are dominated by volcaniclastic deposits, which are significantly more resistant to compaction due to their higher internal strength and grain characteristics (Manga et al., 2025); compaction is therefore assumed negligible for these units. Unit CSK3 comprises mixed lithologies (oozes, sands, and lithified intervals) with variable but overall reduced compaction compared to pure oozes, and we estimate a conservative thickness uncertainty of 10%–15% for this unit.

Despite these limitations, all four approaches reveal generally consistent temporal patterns in deformation, lending confidence that the observed trends reflect genuine tectonic signals rather than methodological artefacts. In particular, the data sets consistently indicate (a) low and relatively uniform deformation rates during early basin development, (b) a basin-wide acceleration fault throw beginning around ∼330 ka, (c) a peak in cumulative fault throw, subsidence and extension rates between the Lower Pumice 1 and 2 eruptions (186–177 ka), (d) a decrease in subsidence and fault throw following the emplacement of the Kos Plateau Tuff, and (e) a second increase in subsidence, extension and fault throw between the Cape Riva and Minoan eruptions (22–4 ka).

During deposition of Unit CSK3 (>2 to ∼1 Ma), accommodation was distributed across several broad depressions, seemingly decoupled from the present-day NE–SW striking tectonic framework (Figures 6g and 6h). The main depocenters extended across what are now major fault structures, for example, from the East Anafi Graben across the Santorini–Anafi Fault toward the Anhydros Ridge (Figures 6g and 6h). Other main depocenters extended from the western Anhydros region toward Ios island across the Ios Fault and across the western Anafi Basin (Figures 6g and 6h). The lithologies recovered from this interval support a setting of low relief and relatively uniform basin-floor gradients: Unit CSK3 comprises predominantly fine-grained oozes and sand–ooze alternations, including shell-bearing siliciclastic sands and conglomerates in the East Anhydros Graben (Site U1589; Druitt et al., 2024c), dolomitic muds and bioclastic limestones in the East Anafi Graben (Site U1592; Kutterolf et al., 2024b), thick successions of dolomitic marl, micrite, and calcareous sandstone in the West Anafi Graben (Site U1599; Druitt et al., 2024e), and organic-rich oozes to calcareous and tuffaceous muds in the West Anhydros Graben (Site U1593; Druitt et al., 2024d). Seismic reflections show well-stratified, largely undisturbed reflections (Figures 3 and 4). Flattening of Horizon csk2c shows that reflections within Unit CSK3 are generally parallel to subparallel in the Kolumbo Graben (Figure 5e), and in the East Anhydros and East Anafi Grabens (Figure S6 in Supporting Information S1). Together, our analyses indicate the deposition of Unit CSK3 in broad, gently subsiding basins.

A major tectonic reorganization is reflected in the sediment distribution of Unit CSK2 (∼1 Ma–190 ka), when the sedimentation shifted into four NE–SW-aligned depocenters: the East Anafi Graben, the West Anhydros Graben, and the smaller East Anhydros and West Anafi Grabens (Figures 6e and 6f). The pronounced thickening of CSK2 toward the Santorini-Anafi Fault in the East Anafi Graben and toward the East Ios Fault in the East Anhydros Graben demonstrates that extension had become focused along discrete normal faults (Figures 3 and 6). This is especially evident for Subunits CSK2c and CSK2b (Archaeos Tuff), which show a distinct thickening toward the East Ios and Santorini-Anafi Faults (Figures 3 and 6). The well-stratified Subunit CSK2a shows a more gradual thickening toward the master faults of the eastern basins (Figures 3 and 6). The thickness maps of Unit CSK2 also reflect a distinct accumulation in the central West Anhydros Graben, which can be partly attributed to the emergence of the early Kolumbo edifice, forming the K1/K2 sequence at ∼265–193 ka (Metcalfe et al., 2026).

Subsidence rates during deposition of Unit CSK2 (0.1–0.8 m kyr^{-1}) are only constrained by the Archaeos and the Lower Pumice 1 megabeds (Figures 7i–7l). Similarly, fault throw rates are generally low between 765 and 330 ka and in the order of 0.1 m kyr^{-1} at the Kolumbo Fault. However, we observe a marked increase in the interval between 330 and ∼186 ka with throw rates increasing by a factor of ∼8 at the Kolumbo Fault. Internal faults within the basins show similar relative increases in throw rates (Figures 8e–8l). In the same interval, we observe

that thickness differences of individual units across the Kolumbo Fault start to become more significant (Figure 5).

During deposition of Unit CSK1 (186 ka–present), sedimentation further localized into a reduced set of active basins (Figures 6c and 6d). Sediment accumulation in the West Anafi Graben largely ceased, while sediment accommodation remained focused in the East Anafi and East Anhydros Grabens (Figures 6c and 6d). The most significant change occurred in the western Anhydros Basin, where subsidence became strongly concentrated in the Kolumbo Graben (Figures 6c and 6d). Sedimentation in this interval is dominated by the emplacement of large silicic megabeds from Modern Santorini and Kos, and eruptions from Kolumbo and the Kolumbo Volcanic Chain infilling the graben structures (Figures 6c and 6d). Additional deposition on structural highs is indicated by the wedge deposits north and east of Santorini, likely representing proximal deposits from Santorini's CFSE activity (arrows in Figure 6d) (Preine, Hübscher, et al., 2022; Preine, Karstens, Hübscher, Nomikou, et al., 2022).

This change is clearly reflected in the seismic images shown in Figures 4 and 5, indicating that the thickness of Unit CSK1 is about 4 times greater on the hanging wall compared to the footwall of the Kolumbo Fault. Our estimates for throw rates at the Kolumbo Fault peak in the interval between the Lower Pumice 1 and 2 eruptions, reaching values of up to ∼3.8 m kyr^{-1} (Figure 8i). These values are likely exaggerated by the thickness differences induced by the emplacement of volcanic megabeds (Figure 8i). Internal faults within the other basins show similar increases in this interval (Figures 8j–8l), and also subsidence rates reach their highest values of up to ∼4.7 m kyr^{-1} in the East Anafi Basin (Figure 7k).

After the emplacement of the Kos Plateau Tuff megabed, throw rates and subsidence rates drop significantly, reaching similar values as in the pre-330 ka interval (Figures 7j and 8i–8l). Although strongly influenced by the overprinting signal of volcanic megabeds, our analysis indicates another increase of throw rates between the formation of Kolumbo edifice K4 and between the Cape Riva and Minoan eruptions (Figures 8i and 8j). Our subsidence and extension rate estimates also indicate increases in this interval, although the uncertainties are considerable (Figures 7i and 7j).

Taken together, these observations indicate a progressive evolution from diffuse early extension (>2 Ma) to increasingly localized deformation within a fault-controlled rift system. This evolution can be summarized in five main phases: (a) low and distributed deformation within a basin geometry distinct from the current structural arrangement (>2 to ∼1 Ma); (b) establishment of NE–SW fault-controlled basins (∼1 Ma to ∼330 ka); (c) basin-wide rift acceleration and strain localization (∼330–186 ka); (d) infilling by volcanic megabeds, accompanied by high throw and subsidence rates (186–161 ka); (e) reduced fault activity from 161 to ∼24 ka; and (f) a second increase in throw and subsidence between ∼24 ka and present-day.

These patterns are consistently expressed across independent data sets, including basin-scale accommodation evolution (Figure 6), subsidence reconstructions (Figure 7), and fault-specific throw histories for both the Kolumbo Fault and intra-basin structures (Figures 5 and 8i–8l), indicating that they reflect a coherent response to regional variations in tectonic stress rather than local or method-dependent effects. While the timing of these patterns is seemingly synchronized across the SATZ, the magnitude of strain is highly partitioned between different structures. After ∼330 ka, deformation began to concentrate more heavily on Kolumbo Graben, whereas older basins like the West Anafi Graben became increasingly less active (Figures 6 and 8). The Kolumbo Graben thus represents the youngest structural element in the system and the most recent stage of strain localization.

5.2. Episodic Deformation and Comparison to Present-Day Extension Rates

In extensional half-graben systems, basin subsidence and fault slip are kinematically linked through block rotation and displacement along normal faults (Leeder & Gawthorpe, 1987). The rotation of volcanic megabeds therefore records the integrated vertical response of the crust to fault-controlled extension, whereas throw rates capture the localized expression of this deformation. The close correspondence between these independent data sets indicates that they reflect a common underlying tectonic deformation on different scales (Figures 7 and 8).

Both subsidence reconstructions and throw rate estimates reveal that deformation within the SATZ was episodic rather than steady (Figures 7 and 8). A pronounced phase of fault throw occurred between ∼330 and 161 ka with fault throw rates increasing by up to an order of magnitude. While our subsidence calculation approach does not allow us to resolve changes around 330 ka, it shows that subsidence rates peak between 186 and 177 ka during which subsidence rates increased by factors of ∼4–8. This acceleration is observed consistently across several

basins and fault systems, indicating that it represents a regional tectonic pulse rather than a localized phenomenon. Following this interval, deformation rates decreased after emplacement of the Kos Plateau Tuff (~161 ka), suggesting a transition to a less active phase of rift evolution. A secondary increase in deformation during the Cape Riva–Minoan interval indicates that such pulses may recur on 10^4–10^5 year timescales.

Comparison with present-day geodetic data provides context for these reconstructed rates. Recent GNSS measurements indicate that the SATZ accommodates horizontal extension on the order of ~2–4 mm yr^{-1} (Briole et al., 2021). Our reconstructed long-term extension rates for the Anafi Basin generally range from ~0.4 to 0.7 mm yr^{-1} during background phases, but surge to ~2.5–4.5 mm yr^{-1} during short-lived peak phases (Figures 7k and 7l). This suggests that during high-activity intervals, a single fault system within the SATZ was capable of accommodating the entire present-day regional extension budget. While such values are high, they are not exceptional in the context of active Aegean rifts. For example, the 1956 Amorgos earthquake produced coseismic displacements of ~10–17 m, demonstrating that large amounts of strain can be released rapidly on individual faults during short-lived events (Leclerc et al., 2024). When averaged over several thousands of years, such behavior is consistent with mm-scale throw rates. Similarly, long-term geological and geodetic observations from the Gulf of Corinth, one of the most rapidly extending continental rifts in Europe, indicate extension rates increasing from ~6 mm yr^{-1} in the east to up to ~16 mm yr^{-1} in the west (e.g., Verroios & Zygouri, 2021). Individual faults within the rift exhibit Late Quaternary slip rates ranging from ~0.3 to 11 mm yr^{-1}, with major fault structures accommodating several mm yr^{-1} on average (Beckers et al., 2015; de Gelder et al., 2019).

What makes the SATZ special is not the absolute magnitudes of deformation rates, but the fact that we can resolve their temporal variability. Our geological record indicates that strain is not continuously distributed across the rift, but instead concentrates during short-lived tectonic pulses that manifest as both basin subsidence and fault slip. This suggests that strain localization and strain rates within the rift system evolve dynamically through time.

5.3. Structural Control of Magma Emplacement

Seismic profiles across the non-volcanic East Anafi and East Anhydros Grabens reveal complex zones of internal faults, most pronounced in the Anafi Basin (Figures 1b and 9a–9c). These structures are synthetic in the northwest and become antithetic toward the southeast, creating localized depressions within the larger half-grabens that are hosting them. We interpret these internal fault zones as part of the progressive evolution of the rift system. Analog models of continental rifting show that as rifting continues, deformation commonly occurs toward the rift axis (Corti, 2012). This evolution produces dense swarms of axial or intra-rift faults and can generate graben-in-graben geometries (Corti, 2012). These internal fault zones accommodate extensional strain within the thinned rift floor. Following this conceptual framework, we propose that the internal faults observed in the East Anafi Graben and the East Anhydros Graben represent the surface expression of this inward migration of deformation, reflecting zones where extension has been accommodated and become concentrated toward the basin center (Figures 9a–9c).

Signal attenuation and reflection distortion are common in seismic images beneath volcanic edifices and result from highly heterogeneous and strongly scattering lithologies in vent-proximal regions, including dikes, lava flows, and welded pyroclastics (Jackson, 2012; Magee et al., 2013; Reynolds et al., 2018). This effect is evident at the isolated volcanic cone in Figure 4f, where the flanks are offset by 40–50 m above the Kolumbo Fault, while the fault itself is obscured beneath the central conduit region, causing a broad zone of acoustic blanking. Similar signal loss is observed beneath Kolumbo and the cones of the Kolumbo Volcanic Chain (Figures 4a, 4c, 4f, and 9d–f), preventing direct imaging of potential faults. Nevertheless, small-scale faults comparable to those in the non-volcanic basins (Figures 3a, 3b, and 9a–c) occur abundantly adjacent to the volcanic edifices. These faults have also been identified in 3D seismic P-cable data near Kolumbo and trend NE–SW, roughly parallel to the Kolumbo Fault (Crutchley et al., 2023).

We compare the distance of internal rift fault zones from their respective basin-bounding faults to the width of each graben (pink bars in Figures 9g and 9h). Although the measurements are approximate due to slight obliquity of some seismic lines, internal fault zones consistently widen with increasing distance from the master fault. This trend is expressed in the contrasting dimensions of mid-graben fault zones in the East Anafi Graben and the East Anhydros Graben (Figures 9g and 9h). We also plot the distance of volcanic edifices from the Kolumbo Fault against the width of the Kolumbo Graben (orange circles in Figures 9g and 9h). Nearly all volcanic edifices fall within the area defined by the interpolated minimum and maximum extent of internal rift fault zones (Figure 9g).

10.1029/2025GC012897

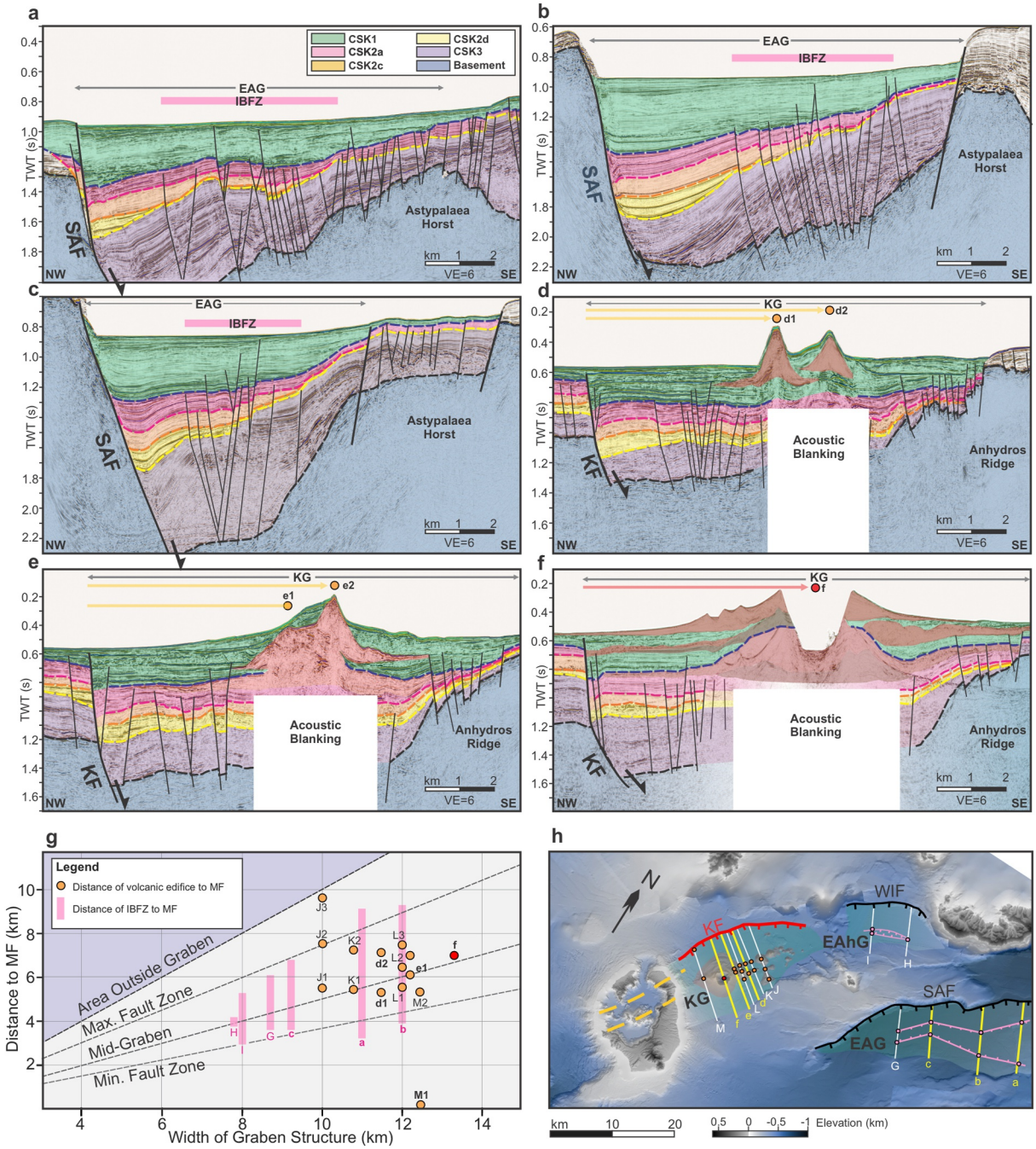

Figure 9. Structural position of intra-basin faults and volcanic edifices within their respective grabens. (a–c) Seismic profiles across the East Anafi Graben (EAG). Semi-transparent colors indicate the main seismostratigraphic units. Solid arrows show the approximate graben width, measured from the Santorini–Anafi Fault (SAF) to the Astypalaea Horst. Pink bars indicate the width of intra-basin fault zones (IBFZ). (d–f) Seismic profiles across the Kolumbo Graben (KG) and the Kolumbo Volcanic Chain (KVC). Solid arrows indicate the width of the Kolumbo Graben, measured from the Kolumbo Fault (KF) to the Anhydros Ridge. Yellow arrows show the distance from the Kolumbo Fault to the approximate center of volcanic edifices. (g) Distances from master faults (MF) to volcanic edifices (orange circles) measured along the profiles shown in (h). Minimum distances are labeled "1," maximum distances "2." The red circle (f) marks the distance between the Kolumbo Fault and Kolumbo. Distances from the master faults to intra-basin fault zones (IBFZ) are highlighted by the pink bars. The upper dashed line indicates the boundary beyond which a structure would lie outside its graben (distance to master fault equals graben width). The central dashed line marks the graben center (distance to master fault equals half of graben width). (h) Rotated morphological map showing the locations of the seismic profiles from panels (a–f) in yellow. Additional profiles used in panel (g) are shown in white (G–M). Black toothed lines mark master faults in non-volcanic basins (West Ios Fault, WIF; Santorini–Anafi Fault, SAF). Red toothed lines mark the Kolumbo Fault. Pink toothed lines mark mid-graben fault zones. Yellow lines trace the Kameni and Kolumbo Lines. The semi-transparent red area highlights the Kolumbo Volcanic Chain; the semi-transparent green area indicates the approximate extents of the East Anhydros Graben (EAhG), East Anafi Graben (EAG), and Kolumbo Graben (KG).

Only two edifices (M1, J3) lie outside this field, one directly on the Kolumbo Fault (M1) and one close to the Anhydros Ridge (J3) (Figures 9g and 9h).

Although the isolated volcanic cone in Figure 4f is clearly aligned above the Kolumbo Fault, the majority of volcanic edifices in the Kolumbo Volcanic Chain are not located along the master fault. Instead, they cluster within the basin interior and occupy the same structural domain as the mid-graben faults in the non-volcanic basins (Figure 9). Seismic profiles show that the Kolumbo Graben contains numerous small-scale faults on both sides of the volcanic edifices of the Kolumbo Volcanic Chain, indicating a wide mid-graben deformation zone (Figures 4a and 4c). This spatial correspondence suggests that volcanism preferentially localizes where extensional strain is accommodated away from the main fault.

As demonstrated in analog models and documented in the East African Rift System, deformation and melt supply tend to migrate toward the rift axis in mature rifts, where axial fault networks create effective pathways for magma ascent and volcanic centers cluster along zones of concentrated faulting (Corti, 2012). This framework could explain why the volcanic centers of the Kolumbo Volcanic Chain do not follow the Kolumbo Fault itself but instead align with the intra-rift fault domain observed in the non-volcanic basins (Figure 9). Although acoustic blanking prevents us from directly imaging faults beneath the volcanic edifices, their consistent spatial relationship with these internal rift structures strongly suggests structural control of volcano emplacement.

We therefore argue that the volcanoes of the Kolumbo Volcanic Chain formed above zones of distributed intra-graben deformation, where extensional strain was accommodated by networks of small-scale faults rather than by the master fault alone. These zones are expected to be characterized by reduced effective horizontal stress and enhanced crustal permeability, providing preferential pathways for magma ascent and explaining the systematic offset of the Kolumbo Volcanic Chain from the Kolumbo Fault (Figures 9g and 9h). Once established, repeated magma and fluid transport through these pathways likely thermally and mechanically weakened the crust, further focusing deformation and reinforcing volcano–tectonic feedbacks. This contrasts with results from seismic anisotropy derived from an active source tomography experiment by Heath et al. (2021), which inferred that porosity from local, oriented cracks is uncorrelated with regions of volcanic activity at 2–3 km depth.

5.4. Relationships Between the Kolumbo Volcanic Chain and Santorini

Our findings support an interpretation in which Kolumbo and the Kolumbo Volcanic Chain developed in strain accommodation zones within the Kolumbo Graben, reflecting a possible structural feedback relationship between the magma pathways and strain focusing (Figure 10). The pronounced temporal correlation between the birth of Kolumbo and the onset of CFSE activity at Santorini a quarter of a million years ago (Metcalfe et al., 2026) requires an evaluation of whether this structural trend continues further beneath Santorini.

Although our seismic data lose resolution beneath Santorini, several observations point to a continuation of the Kolumbo Graben underneath Santorini. First, our mapping reveals a continuous basement rise extending from southeastern Santorini, where basement rocks are exposed, to the Anhydros Ridge ∼80 km to the northeast along the SATZ (Figure 6). The Anhydros Ridge represents the SE boundary of the Kolumbo Graben (Figures 4a, 4c, 5, and 9d–9f) and lies parallel to the Kolumbo Fault (Figures 4a and 4c) that coincides with a NE-SW aligned volcanic corridor that includes the Kolumbo Volcanic Chain, the low P-wave velocity anomaly between Santorini and Kolumbo (McVey et al., 2020), and the Kameni and Kolumbo Lines within the Santorini caldera (Figures 1b and 1c). Dike swarms and small-offset faults in northeastern Santorini (Figure 1c) lie directly along strike of the Kolumbo Volcanic Chain (Druitt et al., 1999; Drymoni et al., 2022). These faults, which have minor offsets in younger eruptive units of the Thera Pyroclastic Formation, show similar geometries and magnitudes of throw to internal rift faults in the non-volcanic basins and within the Kolumbo Graben (Figures 3, 4, and 7) (Druitt et al., 1999; Drymoni et al., 2022). The reduced offsets of faults within Unit CSK1 relative to Units CSK2–3 suggest a comparable temporal evolution, with fault activity partly decreasing after ∼161 ka (Figures 7 and 9). Volcanic activity over the past ∼200 ka has been concentrated in the northern caldera basin, between the Kameni and Kolumbo Lines (Figure 1c) (Druitt et al., 1999). A continuity of the Kolumbo Graben and the internal strain-accommodation zone between the Kolumbo and northern Santorini provides a plausible explanation for this persistent alignment of magmatic pathways at Santorini.

A pre-existing structural depression beneath northwestern Santorini is also reflected in the asymmetric distribution of the Thera Pyroclastic Formation (and stratigraphically interleaved lava successions such as the Skaros

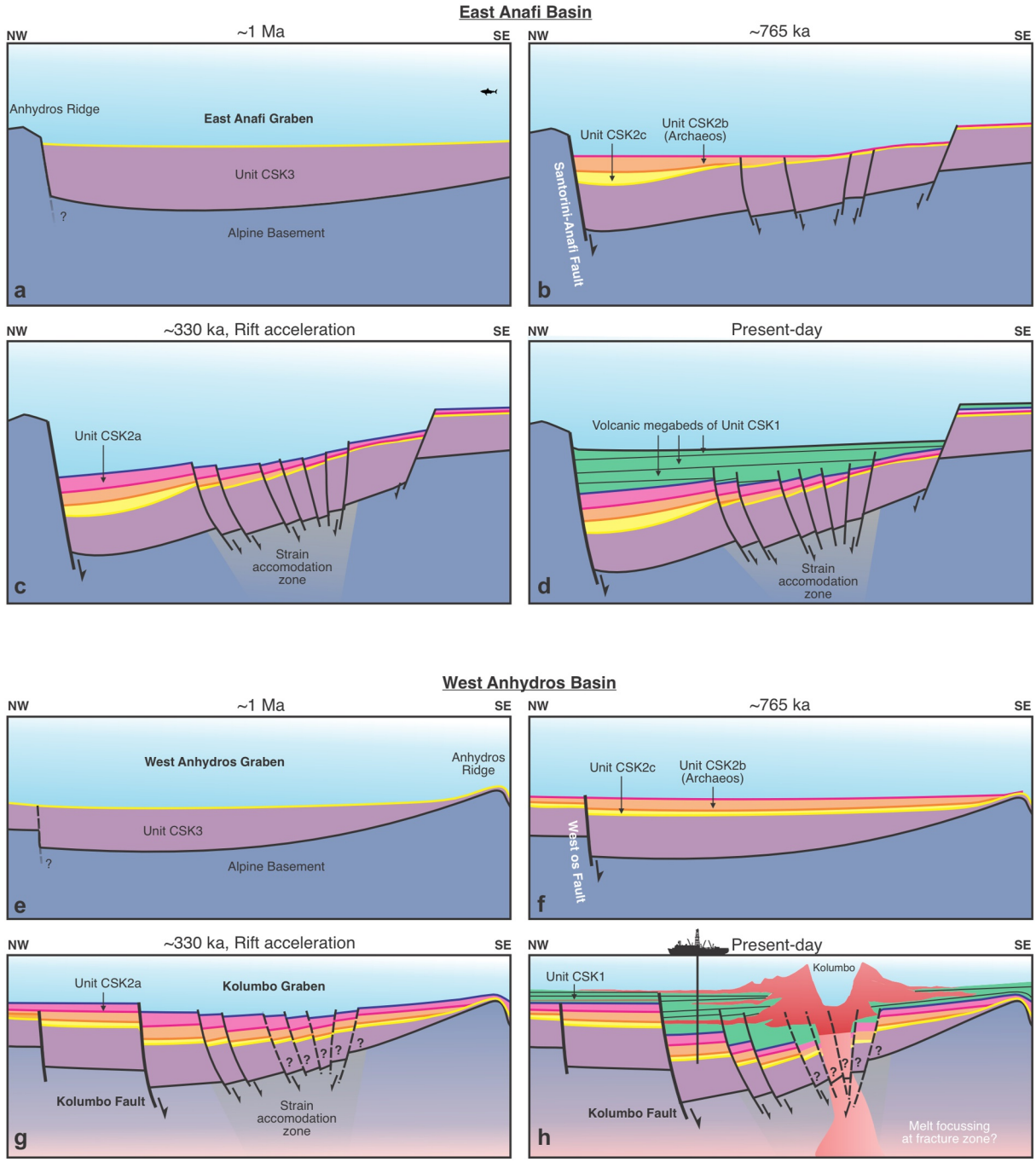

Figure 10. Conceptual model of the volcano–tectonic evolution of the East Anafi and Kolumbo Grabens. (a–d) East Anafi Graben: Semi-continuous deposition of Unit CSK3 between >2 and ~1 Ma (a) was followed by the onset of pronounced NW–SE rifting and subsidence along the Santorini-Anafi Fault, driving the thickening of Subunits CSK2c and CSK2b (Archaeos; b). During deposition of Subunit CSK2a, rifting accelerated at ~330 ka, producing a starved rift with focused subsidence at the Santorini-Anafi Fault and distributed internal deformation within the basin to accommodate strain (c). Continued, but slower, extension during deposition of Unit CSK1 allowed volcanic megabeds to infill the remaining accommodation space (d). (e–h) Kolumbo Graben: Unit CSK3 accumulated within the broad West Anhydros Graben (e). Subunits CSK2c and CSK2b accumulated in a slightly asymmetric basin defined by the West Ios Fault (f). Afterward, the Kolumbo Fault initiated, forming the youngest and most localized rift segment of the Santorini-Amorgos Tectonic Zone. Accelerated subsidence affected the Kolumbo Graben around ~330 ka. We infer that, analogous to the non-volcanic grabens in the region, a basin-internal strain accommodation zone developed in the center of the Kolumbo Graben, marked by the dotted fault zones with question marks (g). After ~265 ka, Kolumbo emerged, progressively filling the graben together with major Santorini-derived volcanic megabeds, rendering the rift structure invisible at the modern seafloor. We speculate that magma may have reached the surface via melt focusing along the basin-internal strain-accommodation zone, which could have provided preferential pathways for melt ascent (h).

or Therasia lavas) onshore Santorini, which are thickest in the northwest and thin southeastward onlapping the Alpine basement (Figure 6) (Druitt et al., 1999). Thick pyroclastic deposits >400 m in the Fira area have been imaged by ambient noise measurements (Chatzis et al., 2022). This pattern is consistent with hanging-wall rotation along a NE-SW oriented fault that generated accommodation space in the northwest and relative uplift to the southeast. Supporting this view, the early submarine products of the Akrotiri volcanic centers (650–550 ka) have been uplifted by several tens of meters in southeastern Santorini (Druitt et al., 1999).

The presence of a NE-SW trending structural depression beneath Santorini is further supported by gravity and magnetic anomalies structural depression beneath northern Santorini, consistent with earlier proposals of a "proto-Anhydros" Basin beneath the island (Budetta et al., 1984; Heath et al., 2019; Heiken & McCoy, 1984). While this basin was previously considered Pliocene or early Pleistocene in age (Heath et al., 2019), our stratigraphic constraints indicate that it may have been significantly deepened by a phase of accelerated subsidence around ∼330 ka. Similar to the Kolumbo Graben, the products of the Thera Pyroclastic Formation and stratigraphically interleaved lava piles would have subsequently filled this depression, explaining why the proto-basin structure is not visible on Santorini at present-day.

5.5. Interactions Between Rifting and the Volcanic-Arc Magmatic System

The relationships between rift extension and the volcanic arc magmatic system in the SATZ raises the fundamental questions of primary controls and feedbacks between the different processes. Studies of continental rift systems such as the East African Rift (Keir et al., 2013; Kounoudis et al., 2025; Maestrelli et al., 2024; Rooney et al., 2025) and the Taupo Volcanic Zone (Gold et al., 2026; Rowland et al., 2010; Wilson et al., 2009) have yielded a detailed conceptual framework for complex interactions and feedbacks (Brune et al., 2023). Lithospheric stretching can increase magma supply rate due to increased mantle melting (Fioraso et al., 2024; Sternai, 2020), shear-enhanced melt segregation, and enhanced crustal permeability (Kohlstedt & Holtzman, 2009; Sparks et al., 2019; Weinberg et al., 2021), and creates space in the crust for intrusions and magma reservoirs. Conversely, an increasing magma supply rate facilitates faster lithospheric extension through strain accommodation, crustal weakening, and fault lubrication (Brune et al., 2023; Keir et al., 2013). Changing regional stresses associated with rifting can also affect magma storage architecture (Ferrante et al., 2024). While these general principles are known, firm constraints are not always available. We therefore review the different lines of evidence for forcings and feedbacks at the SATZ, focusing on the role of the newly discovered Kolumbo Graben.

Following the onset of rifting >2 Ma, the development of the NE-SW SATZ rift system since ∼1 Ma succeeded the activity of Christiana Volcano (2.5–2.7 Ma; Vroon et al., 2025), and coincided approximately with the earliest explosive eruptions of Ancient Santorini (0.94 Ma; Metcalfe et al., 2026). The development of NE-SW rifting occurred in the late Pleistocene across the southern Aegean, resulted from a change in regional stresses and counter-clockwise block rotations, recorded on the island of Rhodos (van Hinsbergen et al., 2007) and in the offshore Rhodos Basin (Hall et al., 2009). An early-to-mid-Pleistocene tectonic reorganization across the broader eastern Mediterranean has been suggested to be related to the incipient continent-continent collision between the Eratosthenes Seamount (Nubian plate) and Cyprus (Eurasian plate) (Schattner, 2010). The new NE-SW striking rift system intersected and overprinted a Miocene/Pleistocene E-W striking tectonic regime (Heath et al., 2019; Preine, Hübscher, et al., 2022). The emergence of Christiana and early Santorini may have been facilitated by the intersection of these two tectonic fabrics (Heath et al., 2019; Preine, Hübscher, et al., 2022). However, it is also possible that the Christiana and early Santorini magmatic systems may have helped focus the strain on that area, forming the SATZ. The few constraints on this early period preclude detailed analysis, but it appears that regional stresses dominated development of the SATZ in this early period.

Following the development of Ancient Santorini and its transition to Modern Santorini (<560 ka), the rate of rifting across the SATZ accelerated, as proposed by Preine, Hübscher, et al. (2022), Preine, Karstens, Hübscher, Nomikou, et al. (2022), Preine, Karstens, Hübscher, Crutchley, et al. (2022), and Metcalfe et al. (2025a) and confirmed in the present study. Elevated rates of subsidence and fault throw began about 330 ka and peaked between 186 and 177 ka across multiple basins. Because the acceleration is recorded in three separate tectonic grabens (East Anhydros, East Anafi, Kolumbo), it was likely driven by an increase in regional extension rate. Our quantification of increasing subsidence and fault throw rates during this period support the idea that the acceleration in rifting drove Santorini into its present state of highly explosive activity that began at ∼250 ka, producing four caldera-forming silicic eruptions since 186 ka, and causing the birth of Kolumbo Volcano (∼265 ka). The increased rate of rifting deepened

the SATZ basins because subsidence rate outpaced sediment supply. The basins then acted as depocenters for the CSFE and Kolumbo megabeds that filled the basins to their present levels (Metcalfe et al., 2025a; Preine, Hübscher, et al., 2022; Preine, Karstens, Hübscher, Nomikou, et al., 2022; Preine, Karstens, Hübscher, Crutchley, et al., 2022). Possible mechanisms by which accelerated extension rates led to increased eruption explosivity include (a) increasing the melt supply from deep storage regions to the crustal magmatic system, (b) increasing crustal permeability, and (c) favoring horizontal magma storage architectures that could trap incoming magmas and lead to thermomechanical runaway and the growth of large reservoirs of eruptible silicic magma (Bouvet de Maisonneuve et al., 2021). Feedbacks may have occurred between crustal softening and accelerated rifting as large magma reservoirs developed. Increased magma supply due to deeper and wider-scale upper-plate processes may also have contributed to increasing rift extension rates. Notably, the Kos Volcano that lies in another Plio-Pleistocene NE-SW rift system on the South Aegean Volcanic Arc (Figure 1a) also had a major CSFE (the Kos Plateau Tuff; 161 ka) in this period. We infer that the phase of accelerated rifting from 330 to 161 ka was primarily of regional tectonic origin, and that feedbacks with the magmatic system were of secondary importance.

As the rifting accelerated, strain localized progressively into the Kolumbo Graben. Although it emerged after 765 ka, the graben deepened markedly during the peak extension phase. A strong relationship between the Kolumbo Graben and magmatism is shown by (a) it's probable passage under the northern caldera basin of Santorini, which contains all major eruptive vents of the last ∼250 ka (Druitt et al., 1999); (b) the coincidence of its geographic footprint with that of the upper crustal magma reservoir that extends NE-SW from Santorini towards Kolumbo (McVey et al., 2020), (c) the presence of Kolumbo and the Kolumbo Volcanic Chain within it, and (d) the presence of a dense swarm of dikes of different ages on the extrapolation of the graben through Santorini (Drymoni et al., 2022). The approximate synchroneity of the onset of highly explosive activity at Santorini (<250 ka) and the birth of Kolumbo Volcano (∼265 ka) may also relate to accelerated development of the Kolumbo Graben. These features jointly suggest strong couplings between tectonics and magmatism in the Kolumbo Graben, whose emergence followed the 765 ka Archaeos eruption created a focused zone of extension in which feedback processes could be amplified. We suggest that faulting in the graben made space for magma storage and ascent to the surface, while the magma bodies and zones of high fluid pressure accommodated strain and fed back into the graben development. In this context, we note the correspondence between the extrapolated Kolumbo Fault and a SE-dipping low-velocity zone extending to ∼4 km depth (Figure S7 in Supporting Information S1), previously interpreted as a thin mush zone linked to a shallow magma body beneath Santorini (McVey et al., 2020). Strain concentration along the fault and within the graben axis may have facilitated lateral migration of ascending melts from the mid-crustal reservoir at 11–13 km depth (Autumn et al., 2025; Hufstetler & Hooft, 2025; Hufstetler et al., 2025) toward the Kolumbo Graben, promoting the development of shallow melt bodies beneath Kolumbo and northern Santorini (Chrapkiewicz et al., 2022; McVey et al., 2020). In this sense, the Kolumbo Graben represents a highly localized manifestation of the tectonic forcing inferred from the distal rift basins, but with additional strain concentration that may have further intensified melt transport beneath both Kolumbo and Santorini. With the onset of highly explosive activity, crustal stress changes resulting from the emptying of magma chambers and caldera collapses (e.g., Corbi et al., 2015) may also have fed back into the growth of the Kolumbo Graben as a major tectonic feature of the volcanic field.

At the same time, our data indicate that peak subsidence and fault throw rates are observed not during the initial acceleration phase but between the Lower Pumice 1 and 2 eruptions, as well as between the Cape Riva and Minoan caldera-forming silicic (Figures 7 and 8). Although uncertainties in our estimates are high in these intervals due to the short timescales involved, the recurrence of these peaks across two independent data sets suggests that deformation may have been amplified at times when large, melt-rich magma reservoirs were present beneath Santorini. Such behavior is consistent with feedbacks between tectonics and magmatism observed in other rift settings (e.g., Brune et al., 2023; Rowland et al., 2010).

Dike intrusion also likely contributed to deformation in the Kolumbo Graben by accommodating strain. The emplacement of shallow dike swarms can generate significant surface extension and faulting, as documented in various volcanic rift zones (Rubin, 1992; Rubin & Pollard, 1988). In this context, it is notable that the ∼4 km width of the eruptive centers in the Kolumbo Volcanic Chain is consistent with numerical models by Rubin (1992), which suggest surface deformation zones above dikes at depths that are a fraction of the deformation width. This spatial scale matches the shallow silicic reservoir identified beneath Kolumbo at depths of 2–5 km (Chrapkiewicz et al., 2022), suggesting that dike-induced dilation may have been a contributor to subsidence along the volcanic chain, especially during peak eruptive phases.

Table 1
Summary of Feedback Mechanisms Between Rift Tectonics (T) and the Volcanic Arc Magmatic System (M) in the Christiana-Santorini-Kolumbo volcanic field Over the Last 1 Ma

Timescale (ka)	Length scale (km)	Tectonic, T Magmatic, M	Regional tectonics	Magmatism	Feedback mechanisms
<1,000	10^2	T >> M	• Regional NE-SW rifting • Counterclockwise crustal rotation	• Birth and growth of Santorini magmatic system	• Magmatism emerging at the intersection of Miocene/Pliocene tectonic regimes?
<330	10^2	T > M	• Acceleration of rifting in all rift basins • Formation of intra-basin fault zones	• Increased explosivity at Santorini • Birth of Kolumbo at ~265 ka • Increased magma supply and eruption rates	• Tectonic-controlled vent localization • Possible feedbacks between magma supply, crustal rheology, and rift extension rates
<190	10–50	T ~ M	• Strain localization in the Kolumbo Graben	• Growth of large magma reservoirs along the graben and its extension • Onset of Santorini caldera-forming silicic eruptions • Birth of the Kolumbo Volcanic Chain • Emplacement of Santorini dike swarms	• Partial accommodation of extension by dikes, melt-rich magma reservoirs and magma shearing • Stress changes due to large eruptions and caldera collapses
<20	10^2	T < M	• Peaks in fault slip and subsidence rates	• Large caldera-forming silicic eruptions	• Amplification of deformation by large, melt-rich magma reservoirs • Stress changes due to large eruptions and caldera collapses
Historical	10	T ~ M	• Seismic swarms, Transient stress triggering	• Vertical movements at Santorini and Kolumbo. • Probable dike injection to NE of Santorini	• Transfers of crustal stresses and possibly fluids between Santorini and Kolumbo

Note. Stages track the transition from regional tectonic rifting to a coupled system where magmatism and caldera-forming events drive crustal deformation and subsidence rates.

In summary, we infer that at large spatial (10^2 km) and temporal (10^5–10^6 ka) scales, tectonics has served to modulate the volcanic arc magmatic system, whereas at progressively smaller scales ($<10^2$ km; $<10^5$ ka) feedbacks between the magmatic system and regional stresses play increasingly important roles, notably in the Kolumbo Graben (Table 1). These feedbacks continue in the area of the Kolumbo Graben today, as manifested by the coupled behaviors of Santorini, Kolumbo and seismic activity during the unrest of 2024–25 (Isken, Karstens et al., 2025; Lomax et al., 2025).

6. Conclusions

Our ground-truthed seismostratigraphic analysis provides new constraints on the tectonic evolution of the Santorini–Amorgos Tectonic Zone (SATZ) and its role in modulating magma ascent and eruption at Santorini and Kolumbo. The main findings are:

1. Identification of a new rift structure.
   We identify the previously unrecognized Kolumbo Graben, a NE–SW–striking asymmetric graben, bound by a blind normal fault with ~220 m of displacement. This structure fundamentally revises the tectonic architecture of the SATZ, placing Kolumbo and the Kolumbo Volcanic Chain at the center of a young, highly localized rift segment.
2. Episodic rift evolution and strain localization.
   Rift development and evolution occurred in multiple phases, with a key transition at ~330 ka marked by a basin-wide acceleration in deformation, including the initiation of the Kolumbo Fault. Slip and subsidence rates increased by factors of ~3 to >10 during this phase, indicating that deformation was episodic with short-lived pulses of accelerated extension.
3. Structural control on magma ascent.
   Volcanic centers of the Kolumbo Volcanic Chain do not align with the master fault but cluster within the graben interior. We argue that the Kolumbo Graben, like the other grabens, was affected by internal

deformation to accommodate extensional strain and these structures acted as preferred magma pathways once rifting became strongly localized.

4. The Kolumbo Graben likely extends beneath Santorini.
   Structural continuity, basin geometry, and volcanic lineaments indicate a continuation of the Kolumbo Graben beneath Santorini's northern caldera, subsequently filled and overprinted by the eruptive products from Modern Santorini.
5. Tectonic forcing primed both volcanic systems.
   Accelerated rifting around ~330 ka preceded both the emergence of Kolumbo and the beginning of repeated caldera-forming silicic eruptions at Modern Santorini at ~250 ka. We infer that changes in crustal stress, permeability, and fault-related shearing within the Kolumbo Graben modulated melt segregation and ascent within the transcrustal magmatic system. While tectonic-magmatic feedbacks likely enhanced strain localization, regional extension acted as the dominant control on system evolution.

Conflict of Interest

The authors declare no conflicts of interest relevant to this study.

Availability Statement

This study utilizes openly accessible DEM data, supplemented by EMODnet and PROTEUS data sets. These resources are available through the EMODnet Bathymetry Portal at https://portal.emodnet-bathymetry.eu, (Thierry et al., 2019) and can be retrieved from https://doi.org/10.12770/18ff0d48-b203-4a65-94a9-5fd8b0ec35f6. High-resolution seismic reflection profiles from the POS538 expedition are accessible via Karstens and Preine (2023). Vintage seismic profiles relevant to this study are publicly available at the Marine Geoscience Data System (MGDS) via Hübscher and Preine (2022) and Hübscher et al. (2020). The PROTEUS geophysical data suite, seismic data from MGL1521 and the published velocity models are available via Hooft (2015) and Hufstetler and Hooft (2025), respectively.

Acknowledgments
The International Ocean Discovery Program (IODP) provided the samples and data for this study. We are grateful to the technical team aboard the RV JOIDES Resolution for their dedicated work during Expedition 398, and to all crew members for contributing to a memorable and productive experience. Furthermore, we acknowledge the IODP member organizations for their financial backing and the Municipality of Thera for their assistance with expedition preparations. We extend our thanks to the captains and crews of the RV Poseidon Expeditions POS338 and POS538, as well as the RV Merian Expedition MSM132 and MSM135. J.P. was funded by the German Research Foundation (Grant Hu698/27) and the Woods Hole Oceanographic Institute Postdoctoral Scholarship Program. K.P. and S.K. were funded by the German Research Foundation (Grant KU2685/17-1), and A.M. by the ClerVolc program of Clermont-Auvergne University and by IODP France. The PROTEUS data collection on cruise MGL1521 and analysis were funded by the US National Science Foundation (OCE Grants 14-59794 and 16-07104). The JRSO and Expedition 403 were funded by NSF OCE award 1326927. This is contribution no. 758 of the ClerVolc program of Clermont-Auvergne University. We acknowledge financial support from the Open Access Publication Fund of Universität Hamburg. We are grateful to IHS Markit for providing KINGDOM seismic interpretation software. We thank the Editor, the Associate Editor, Neil C. Mitchell, and an anonymous reviewer for their constructive comments, which helped improve the quality of the manuscript.

References

Anastasakis, G., & Piper, D. J. (2005). Late Neogene evolution of the western South Aegean volcanic arc: Sedimentary imprint of volcanicity around Milos. *Marine Geology*, *215*(3–4), 135–158. https://doi.org/10.1016/j.margeo.2004.11.014

Autumn, K. R., Hooft, E. E., & Toomey, D. R. (2025). Exploring mid-to-lower crustal magma plumbing of Santorini and Kolumbo volcanoes using PmP tomography. *Geochemistry, Geophysics, Geosystems*, *26*(4), e2025GC012170. https://doi.org/10.1029/2025gc012170

Beckers, A., Hubert-Ferrari, A., Beck, C., Bodeux, S., Tripsanas, E., Sakellariou, D., & De Batist, M. (2015). Active faulting at the western tip of the Gulf of Corinth, Greece, from high-resolution seismic data. *Marine Geology*, *360*, 55–69. https://doi.org/10.1016/j.margeo.2014.12.003

Beethe, S., Schmitt, A. K., Koppers, A. A., Pank, K., Metcalfe, A., Druitt, T. H., et al. (2025). New Age for the Archaeos Tuff: Using $^{40}Ar/^{39}Ar$ and U-Pb to Redefine Ancestral Santorini's Tephrochronostratigraphy and Implications for Rapid Magma Accumulation. In *EGU General Assembly Conference Abstracts* (pp. EGU25–12976).

Berndt, C., Campbell, M., Crutchley, G., Karstens, J., Kwasnitschka, T., Nomikou, P., et al. (2025). Monitoring of deformation at Kolumbo Volcano during MULTI-MAREX Cruise 1, Cruise No. MSM132, 3.12. 2024-2.1. 2024, Catania (Italy)-Heraklion (Greece), MMC-1.

Biggs, J., Ayele, A., Fischer, T. P., Fontijn, K., Hutchison, W., Kazimoto, E., et al. (2021). Volcanic activity and hazard in the East African Rift Zone. *Nature communications*, *12*(1), 6881. https://doi.org/10.1038/s41467-021-27166-y

Bouvet de Maisonneuve, C., Forni, F., & Bachmann, O. (2021). Magma reservoir evolution during the build up to and recovery from caldera-forming eruptions—A generalizable model? *Earth-Science Reviews*, *218*, 103684. https://doi.org/10.1016/j.earscirev.2021.103684

Briole, P., Ganas, A., Elias, P., & Dimitrov, D. (2021). The GPS velocity field of the Aegean. New observations, contribution of the earthquakes, crustal blocks model. *Geophysical Journal International*, *226*(1), 468–492. https://doi.org/10.1093/gji/ggab089

Brown, M., Rushmer, T., & Sawyer, E. W. (1995). Introduction to special section: Mechanisms and consequences of melt segregation from crustal protoliths. *Journal of Geophysical Research*, *100*(B8), 15551–15563. https://doi.org/10.1029/95JB01253

Brune, S., Kolawole, F., Olive, J. A., Stamps, D. S., Buck, W. R., Buiter, S. J., et al. (2023). Geodynamics of continental rift initiation and evolution. *Nature Reviews Earth & Environment*, *4*(4), 235–253. https://doi.org/10.1038/s43017-023-00391-3

Buck, W. R. (2004). Consequences of asthenospheric variability on continental rifting. In *Rheology and deformation of the lithosphere at continental margins* (pp. 1–30). Columbia University Press.

Budetta, G., Condarelli, D., Fytikas, M., Kolios, N., Pascale, G., Rapolla, A., & Pinna, E. (1984). Geophysical prospecting on the Santorini Islands. *Bulletin Volcanologique*, *47*(3), 447–466. https://doi.org/10.1007/bf01961218

Carey, S., Nomikou, P., Bell, K. C., Lilley, M., Lupton, J., Roman, C., et al. (2013). CO_2 degassing from hydrothermal vents at Kolumbo submarine volcano, Greece, and the accumulation of acidic crater water. *Geology*, *41*(9), 1035–1038. https://doi.org/10.1130/g34286.1

Cas, R., Giordano, G., & Wright, J. V. (2024). *Volcanology. Processes, deposits, geology and resources* (p. 1833). Springer.

Chatzis, N., Papazachos, C., Theodoulidis, N., Hatzidimitriou, P., Vougioukalakis, G., Paulatto, M., et al. (2022). Metamorphic bedrock geometry of Santorini using HVSR information and geophysical modeling of ambient noise and active-source surface-wave data. *Journal of Volcanology and Geothermal Research*, *432*, 107692. https://doi.org/10.1016/j.jvolgeores.2022.107692

Chrapkiewicz, K., Paulatto, M., Heath, B. A., Hooft, E. E. E., Nomikou, P., Papazachos, C. B., et al. (2022). Magma chamber detected beneath an arc volcano with full-waveform inversion of active-source seismic data. *Geochemistry, Geophysics, Geosystems*, *23*(11), e2022GC010475. https://doi.org/10.1029/2022gc010475

Corbi, F., Rivalta, E., Pinel, V., Maccaferri, F., Bagnardi, M., & Acocella, V. (2015). How caldera collapse shapes the shallow emplacement and transfer of magma in active volcanoes. *Earth and Planetary Science Letters*, *431*, 287–293. https://doi.org/10.1016/j.epsl.2015.09.028

Corti, G. (2012). Evolution and characteristics of continental rifting: Analog modeling-inspired view and comparison with examples from the East African Rift System. *Tectonophysics*, *522*, 1–33. https://doi.org/10.1016/j.tecto.2011.06.010

Crutchley, G. J., Karstens, J., Preine, J., Hübscher, C., Fossen, H., & Kühn, M. (2023). Extensional faulting around Kolumbo Volcano, Aegean Sea—Relationships between local stress fields, fault relay ramps, and volcanism. *Tectonics*, *42*(10), e2023TC007951. https://doi.org/10.1029/2023tc007951

de Gelder, G., Fernández-Blanco, D., Melnick, D., Duclaux, G., Bell, R. E., Jara-Muñoz, J., et al. (2019). Lithospheric flexure and rheology determined by climate cycle markers in the Corinth Rift. *Scientific Reports*, *9*(1), 4260. https://doi.org/10.1038/s41598-018-36377-1

Druitt, T., Kutterolf, S., Ronge, T. A., Hübscher, C., Nomikou, P., Preine, J., et al. (2024a). Giant offshore pumice deposit records a shallow submarine explosive eruption of ancestral Santorini. *Communications Earth & Environment*, *5*(1), 24. https://doi.org/10.1038/s43247-023-01171-z

Druitt, T. H., Edwards, L., Mellors, R. M., Pyle, D. M., Sparks, R. S. J., Lanphere, M., et al. (1999). Santorini volcano. *Geological Society*, *19*(1).

Druitt, T. H., Kutterolf, S., Ronge, T. A., Beethe, S., Bernard, A., Berthod, C., et al. (2024b). Expedition 398 summary. *Proceedings of the International Ocean Discovery Program Expedition reports*, *398*(101).

Druitt, T. H., Kutterolf, S., Ronge, T. A., Beethe, S., Bernard, A., Berthod, C., et al. (2024c). Site U1589. *Proceedings of the International Ocean Discovery Program Expedition reports*, *398*(103).

Druitt, T. H., Kutterolf, S., Ronge, T. A., Beethe, S., Bernard, A., Berthod, C., et al. (2024d). Site U1593. *Proceedings of the International Ocean Discovery Program Expedition reports*, *398*(103).

Druitt, T. H., Kutterolf, S., Ronge, T. A., Beethe, S., Bernard, A., Berthod, C., et al. (2024e). Site U1599. *Proceedings of the International Ocean Discovery Program Expedition reports*, *398*(103).

Drymoni, K., Browning, J., & Gudmundsson, A. (2022). Spatial and temporal volcanotectonic evolution of Santorini volcano, Greece. *Bulletin of Volcanology*, *84*(6), 60. https://doi.org/10.1007/s00445-022-01566-4

Ferrante, G., Rivalta, E., & Maccaferri, F. (2024). Spatio-temporal evolution of rift volcanism controlled top-down by a deepening graben. *Earth and Planetary Science Letters*, *629*, 118593. https://doi.org/10.1016/j.epsl.2024.118593

Fioraso, M., Sternai, P., Olivetti, V., Balestrieri, M. L., Zattin, M., & Cornamusini, G. (2024). Miocene climate cooling and aridification of Antarctica may have enhanced syn-extensional magmatism in the western Ross Sea. *Global and Planetary Change*, *240*, 104538. https://doi.org/10.1016/j.gloplacha.2024.104538

Gautier, P., & Brun, J. P. (1994). Crustal-scale geometry and kinematics of late-orogenic extension in the central Aegean (Cyclades and Ewia Island). *Tectonophysics*, *238*(1–4), 399–424. https://doi.org/10.1016/0040-1951(94)90066-3

Gawthorpe, R. T., & Leeder, M. R. (2000). Tectono-sedimentary evolution of active extensional basins. *Basin Research*, *12*(3-4), 195–218. https://doi.org/10.1111/j.1365-2117.2000.00121.x

Gold, A. S., Snowden, M., Muirhead, J. D., Villamor, P., Coffey, G. L., Wilson, C. J., & Morgenstern, R. (2026). Large-scale rift-related faulting linked to a caldera-forming eruption: A case study from Taupō, New Zealand. *Journal of Volcanology and Geothermal Research*, *469*, 108481. https://doi.org/10.1016/j.jvolgeores.2025.108481

Hall, J., Aksu, A. E., Yaltırak, C., & Winsor, J. D. (2009). Structural architecture of the Rhodes Basin: A deep depocentre that evolved since the Pliocene at the junction of Hellenic and Cyprus Arcs, eastern Mediterranean. *Marine Geology*, *258*(1–4), 1–23.

Heath, B. A., Hooft, E. E. E., Toomey, D. R., Papazachos, C. B., Nomikou, P., Paulatto, M., et al. (2019). Tectonism and its relation to magmatism around Santorini Volcano from upper crustal P wave velocity. *Journal of Geophysical Research: Solid Earth*, *124*(10), 10610–10629. https://doi.org/10.1029/2019jb017699

Heath, B. A., Hooft, E. E. E., Toomey, D. R., Paulatto, M., Papazachos, C. B., Nomikou, P., & Morgan, J. V. (2021). Relationship between active faulting/fracturing and magmatism around Santorini: Seismic anisotropy from an active source tomography experiment. *Journal of Geophysical Research: Solid Earth*, *126*(8), e2021JB021898. https://doi.org/10.1029/2021jb021898

Heiken, G., & McCoy, F., Jr. (1984). Caldera development during the minoan eruption, thira, cyclades, Greece. *Journal of Geophysical Research*, *89*(B10), 8441–8462. https://doi.org/10.1029/JB089iB10p08441

Hooft, E. E. (2015). Crustal Magma Plumbing of the Santorini Volcanic System [Dataset]. *International Federation of Digital Seismograph Networks*. https://doi.org/10.7914/SN/1E_2015

Hooft, E. E., Nomikou, P., Toomey, D. R., Lampridou, D., Getz, C., Christopoulou, M. E., et al. (2017). Backarc tectonism, volcanism, and mass wasting shape seafloor morphology in the Santorini-Christiana-Amorgos region of the Hellenic Volcanic Arc. *Tectonophysics*, *712*, 396–414. https://doi.org/10.1016/j.tecto.2017.06.005

Hooft, E. E. E., Heath, B. A., Toomey, D. R., Paulatto, M., Papazachos, C. B., Nomikou, P., et al. (2019). Seismic imaging of Santorini: Subsurface constraints on caldera collapse and present-day magma recharge. *Earth and Planetary Science Letters*, *514*, 48–61. https://doi.org/10.1016/j.epsl.2019.02.033

Hübscher, C., Preine, J., Schwarz, B., & Bauer, A. (2020). Processed seismic data for seismic line 11 across the Santorini-Amorgos Tectonic Zone from Poseidon cruise POS338 (2006). *Marine Geoscience Data System (MGDS)*. https://doi.org/10.26022/IEDA/327525

Hübscher, C., & Preine, J. (2022). Processed seismic profiles 02, 11, and 15 (SEG-Y format) across the Santorini-Amorgos Tectonic Zone from Poseidon cruise POS338 (2006). *Marine Geoscience Data System (MGDS)*. https://doi.org/10.26022/IEDA/331028

Hübscher, C., Gross, F., Kutterolf, S., Dittmers, C., Eisermann, O., et al. (2025). Investigating extreme geological events along the Aegean Volcanic Arc and Crete's submarine slopes during MULTI-MAREX Cruise 2, Cruise No. MSM135, 05.03.2025–17.04.2025, Malaga (Spain)—Malaga (Spain) (Englisch)[.

Hübscher, C., Hensch, M., Dahm, T., Dehghani, A., Dimitriadis, I., Hort, M., & Taymaz, T. (2006). Toward a risk assessment of central Aegean volcanoes. *Eos, Transactions American Geophysical Union*, *87*(39), 401–407. https://doi.org/10.1029/2006eo390002

Hübscher, C., Ruhnau, M., & Nomikou, P. (2015). Volcano-tectonic evolution of the polygenetic Kolumbo submarine volcano/Santorini (Aegean Sea). *Journal of Volcanology and Geothermal Research*, *291*, 101–111. https://doi.org/10.1016/j.jvolgeores.2014.12.020

Hufstetler, R. S., & Hooft, E. E. (2025). 3-D tomographic P- and S-wave seismic velocity model of the Santorini-Kolumbo Volcanic system (MGL1521, 2015). *Marine Geoscience Data System (MGDS)*. https://doi.org/10.60521/332269

Hufstetler, R. S., Hooft, E. E., Toomey, D. R., VanderBeek, B. P., Papazachos, C. B., & Chatzis, N. (2025). Seismic structure of the mid to upper crust at the Santorini-Kolumbo Magma System from joint earthquake and active source Vp-Vs tomography. *Geochemistry, Geophysics, Geosystems*, *26*(4), e2024GC012022. https://doi.org/10.1029/2024gc012022

Hughes, G. R., & Mahood, G. A. (2011). Silicic calderas in arc settings: Characteristics, distribution, and tectonic controls. *Bulletin*, *123*(7–8), 1577–1595. https://doi.org/10.1130/b30232.1

Isken, M. P., Karstens, J., Nomikou, P., Parks, M. M., Drouin, V., Rivalta, E., et al. (2025). Volcanic crisis reveals coupled magma system at Santorini and Kolumbo. *Nature*, *645*(8082), 939–945. https://doi.org/10.1038/s41586-025-09525-7

Jackson, C. A. L. (2012). Seismic reflection imaging and controls on the preservation of ancient sill-fed magmatic vents. *Journal of the Geological Society*, *169*(5), 503–506. https://doi.org/10.1144/0016-76492011-147

Jolivet, L. (2001). A comparison of geodetic and finite strain pattern in the Aegean, geodynamic implications. *Earth and Planetary science letters*, *187*(1–2), 95–104. https://doi.org/10.1016/s0012-821x(01)00277-1

Karstens, J., Crutchley, G., Elger, J., Kühn, M., Schmid, F., Dalla Valle, G., et al. (2020). R/V Poseidon Cruise Report 538-THESEUS Tsunami hazard of explosive submarine eruptions, 7th October–28th October 2019, Cartagena (Spain)-Heraklion (Greece).

Karstens, J., Crutchley, G. J., Hansteen, T. H., Preine, J., Carey, S., Elger, J., et al. (2023a). Cascading events during the 1650 tsunamigenic eruption of Kolumbo volcano. *Nature Communications*, *14*(1), 6606. https://doi.org/10.1038/s41467-023-42261-y

Karstens, J., & Preine, J. (2023). 2D seismic reflection data from POSEIDON cruise POS538, offshore Santorini [Dataset]. *PANGAEA*. https://doi.org/10.1594/PANGAEA.956579

Karstens, J., Preine, J., Carey, S., Bell, K. L., Nomikou, P., Hübscher, C., et al. (2023b). Formation of undulating seafloor bedforms during the Minoan eruption and their implications for eruption dynamics and slope stability at Santorini. *Earth and Planetary Science Letters*, *616*, 118215. https://doi.org/10.1016/j.epsl.2023.118215

Karstens, J., Preine, J., Crutchley, G. J., Kutterolf, S., van der Bilt, W. G., Hooft, E. E., et al. (2023c). Revised Minoan eruption volume as benchmark for large volcanic eruptions. *Nature communications*, *14*(1), 2497. https://doi.org/10.1038/s41467-023-38176-3

Keir, D., Bastow, I. D., Pagli, C., & Chambers, E. L. (2013). The development of extension and magmatism in the Red Sea rift of Afar. *Tectonophysics*, *607*, 98–114. https://doi.org/10.1016/j.tecto.2012.10.015

Kohlstedt, D. L., & Holtzman, B. K. (2009). Shearing melt out of the Earth: An experimentalist's perspective on the influence of deformation on melt extraction. *Annual Review of Earth and Planetary Sciences*, *37*(1), 561–593. https://doi.org/10.1146/annurev.earth.031208.100104

Kokkalas, S., & Aydin, A. (2013). Is there a link between faulting and magmatism in the south-central Aegean Sea? *Geological Magazine*, *150*(2), 193–224. https://doi.org/10.1017/s0016756812000453

Kounoudis, R., Bastow, I. D., Ebinger, C. J., Goes, S., Zhou, P., Musila, M., et al. (2025). The importance of past rifting in large igneous province development. *Nature*, *647*(8088), 115–120. https://doi.org/10.1038/s41586-025-09668-7

Kutterolf, S., Druitt, T. H., Ronge, T. A., Beethe, S., Bernard, A., Berthod, C., et al. (2024a). Expedition 398 methods. *Proceedings of the International Ocean Discovery Program Expedition reports*, *398*(102).

Kutterolf, S., Druitt, T. H., Ronge, T. A., Beethe, S., Bernard, A., Berthod, C., et al. (2024b). Site U1592. *Proceedings of the International Ocean Discovery Program Expedition reports*, *398*(106).

Kutterolf, S., Druitt, T. H., Ronge, T. A., Beethe, S., Bernard, A., Berthod, C., et al. (2024c). Site U1592. *Proceedings of the International Ocean Discovery Program Expedition reports*, *398*(106).

Kutterolf, S., Freundt, A., Druitt, T. H., McPhie, J., Nomikou, P., Pank, K., et al. (2021). The medial offshore record of explosive volcanism along the central to eastern Aegean Volcanic Arc: 2. Tephra ages and volumes, eruption magnitudes and marine sedimentation rate variations. *Geochemistry, Geophysics, Geosystems*, *22*(12), e2021GC010011. https://doi.org/10.1029/2021gc010011

Kutterolf, S., Freundt, A., Hansteen, T. H., Dettbarn, R., Hampel, F., Sievers, C., et al. (2021). The Medial Offshore Record of Explosive Volcanism Along the Central to Eastern Aegean Volcanic Arc: 1. Tephrostratigraphic Correlations. *Geochemistry, Geophysics, Geosystems*, *22*(12), e2021GC010010. https://doi.org/10.1029/2021gc010010

Leclerc, F., Palagonia, S., Feuillet, N., Nomikou, P., Lampridou, D., Barrière, P., et al. (2024). Large seafloor rupture caused by the 1956 Amorgos tsunamigenic earthquake, Greece. *Communications Earth & Environment*, *5*(1), 663. https://doi.org/10.1038/s43247-024-01839-0

Leeder, M. R., & Gawthorpe, R. L. (1987). Sedimentary models for extensional tilt-block/half-graben basins. *Geological Society, London, Special Publications*, *28*(1), 139–152. https://doi.org/10.1144/gsl.sp.1987.028.01.11

Le Pichon, X., & Angelier, J. (1979). The Hellenic arc and trench system: A key to the neotectonic evolution of the eastern Mediterranean area. *Tectonophysics*, *60*(1–2), 1–42. https://doi.org/10.1016/0040-1951(79)90131-8

Le Pichon, X., & Kreemer, C. (2010). The Miocene-to-present kinematic evolution of the Eastern Mediterranean and Middle East and its implications for dynamics. *Annual Review of Earth and Planetary Sciences*, *38*(1), 323–351. https://doi.org/10.1146/annurev-earth-040809-152419

Lomax, A., Anagnostou, V., Karakostas, V., Hicks, S. P., & Papadimitriou, E. (2025). The 2025 Santorini unrest unveiled: Rebounding magmatic dike intrusion with triggered seismicity. *Science*, *390*(6775), eadz8538. https://doi.org/10.1126/science.adz8538

Maestrelli, D., Corti, G., Bonini, M., Keir, D., Facincani, P., Vannucchi, P., et al. (2024). Fault reactivation and growth at rift-related calderas. *Earth and Planetary Science Letters*, *636*, 118700. https://doi.org/10.1016/j.epsl.2024.118700

Magee, C., Hunt-Stewart, E., & Jackson, C. A. L. (2013). Volcano growth mechanisms and the role of sub-volcanic intrusions: Insights from 2D seismic reflection data. *Earth and Planetary Science Letters*, *373*, 41–53. https://doi.org/10.1016/j.epsl.2013.04.041

Mahony, S. H., Wallace, L. M., Miyoshi, M., Villamor, P., Sparks, R. S. J., & Hasenaka, T. (2011). Volcano-tectonic interactions during rapid plate-boundary evolution in the Kyushu region, SW Japan. *Bulletin*, *123*(11–12), 2201–2223. https://doi.org/10.1130/b30408.1

Manga, M., Wright, V., Cadena, T., McIntosh, I., Preine, J., Tominaga, M., et al. (2025). Contrasting seismic velocity and compaction of marine calcareous oozes and volcaniclastic deposits on the South Aegean Volcanic Arc. *Geochemistry, Geophysics, Geosystems*, *26*(9), e2025GC012327. https://doi.org/10.1029/2025gc012327

McVey, B. G., Hooft, E. E. E., Heath, B. A., Toomey, D. R., Paulatto, M., Morgan, J. V., et al. (2020). Magma accumulation beneath Santorini volcano, Greece, from P-wave tomography. *Geology*, *48*(3), 231–235. https://doi.org/10.1130/g47127.1

Metcalfe, A., Druitt, T., Pank, K., Kutterolf, S., Preine, J., Beethe, S., et al. (2025a). Tectonic modulation of caldera volcanism on the South Aegean Volcanic Arc. *Earth and Planetary Science Letters*, *671*, 119633. Brown & White, 1995. https://doi.org/10.1016/j.epsl.2025.119633

Metcalfe, A., Druitt, T., Pank, K., Kutterolf, S., Preine, J., Kelfoun, K., et al. (2025b). Submarine ash megabed fed by far-traveled, shoreline-crossing pyroclastic currents from a large explosive volcanic eruption. *Science Advances*, *11*(33), eads9642. https://doi.org/10.1126/sciadv.ads9642

Metcalfe, A., Pank, K., Druitt, T. H., Kutterolf, S., Preine, J., Nomikou, P., & IODP, E. T. N. E. S. (2026). Temporal linkages of explosive activity of Kolumbo and Santorini Volcanoes (Greece). *Geology*.

Nomikou, P., Hübscher, C., & Carey, S. (2019). The Christiana–Santorini–kolumbo volcanic field. *Elements: An International Magazine of Mineralogy, Geochemistry, and Petrology*, *15*(3), 171–176. https://doi.org/10.2138/gselements.15.3.171

Nomikou, P., Hübscher, C., Papanikolaou, D., Farangitakis, G. P., Ruhnau, M., & Lampridou, D. (2018). Expanding extension, subsidence and lateral segmentation within the Santorini-Amorgos basins during Quaternary: Implications for the 1956 Amorgos events, central-south Aegean Sea, Greece. *Tectonophysics*, *722*, 138–153. https://doi.org/10.1016/j.tecto.2017.10.016

Nomikou, P., Hübscher, C., Ruhnau, M., & Bejelou, K. (2016). Tectono-stratigraphic evolution through successive extensional events of the Anydros Basin, hosting Kolumbo volcanic field at the Aegean Sea, Greece. *Tectonophysics*, *671*, 202–217. https://doi.org/10.1016/j.tecto.2016.01.021

Nomikou, P., Papanikolaou, D., Alexandri, M., Sakellariou, D., & Rousakis, G. (2013). Submarine volcanoes along the Aegean volcanic arc. *Tectonophysics*, *597*, 123–146. https://doi.org/10.1016/j.tecto.2012.10.001

Nunns, A. G. (1991). Structural restoration of seismic and geologic sections in extensional regimes. *AAPG bulletin*, *75*(2), 278–297. https://doi.org/10.1306/0c9b27a9-1710-11d7-8645000102c1865d

Papazachos, C. B. (2019). Deep structure and active tectonics of the South Aegean volcanic arc. Elements: An International Magazine of Mineralogy. *Geochemistry, and Petrology*, *15*(3), 153–158. https://doi.org/10.2138/gselements.15.3.153

Pe-Piper, G., & Piper, D. J. (2007). Neogene backarc volcanism of the Aegean: New insights into the relationship between magmatism and tectonics.

Pe-Piper, G., & Piper, D. J. W. (2005). The South Aegean active volcanic arc: Relationships between magmatism and tectonics. In *Developments in volcanology* (Vol. 7, pp. 113–133). Elsevier. https://doi.org/10.1016/s1871-644x(05)80034-8

Preine, J., Crutchley, G., Hübscher, C., Manga, M., Tominaga, M., Beethe, S., et al. (2025). *Data report: core-seismic integration and time-depth relationships at IODP Expedition 398 Hellenic Arc Volcanic Field sites*. Texas A & M University.

Preine, J., Hübscher, C., Karstens, J., & Nomikou, P. (2022). Volcano-Tectonic Evolution of the Christiana-Santorini-Kolumbo Rift Zone. *Tectonics*, *41*(11), e2022TC007524. https://doi.org/10.1029/2022tc007524

Preine, J., Karstens, J., Hübscher, C., Crutchley, G. J., Druitt, T. H., Schmid, F., & Nomikou, P. (2022). The Hidden Giant: How a rift pulse triggered a cascade of sector collapses and voluminous secondary mass-transport events in the early evolution of Santorini. *Basin Research*, *34*(4), 1465–1485. https://doi.org/10.1111/bre.12667

Preine, J., Karstens, J., Hübscher, C., Druitt, T., Kutterolf, S., Nomikou, P., et al. (2024). Hazardous explosive eruptions of a recharging multi-cyclic island arc caldera. *Nature Geoscience*, *17*(4), 323–331. https://doi.org/10.1038/s41561-024-01392-7

Preine, J., Karstens, J., Hübscher, C., Nomikou, P., Schmid, F., Crutchley, G. J., et al. (2022). Spatio-temporal evolution of the Christiana-Santorini-Kolumbo volcanic field, Aegean Sea. *Geology*, *50*(1), 96–100. https://doi.org/10.1130/g49167.1

Preine, J., Schwarz, B., Bauer, A., & Huebscher, C. (2020). When There is no offset: A demonstration of seismic diffraction imaging and depth-velocity model building in the southern Aegean Sea. *Journal of Geophysical Research: Solid Earth*, *125*(9), e2020JB019961. https://doi.org/10.1029/2020jb019961

Pyle, D. M., & Elliott, J. R. (2006). Quantitative morphology, recent evolution, and future activity of the Kameni Islands volcano, Santorini, Greece. *Geosphere*, *2*(5), 253–268. https://doi.org/10.1130/ges00028.1

Reynolds, P., Schofield, N., Brown, R. J., & Holford, S. P. (2018). The architecture of submarine monogenetic volcanoes–insights from 3D seismic data. *Basin Research*, *30*(S1), 437–451. https://doi.org/10.1111/bre.12230

Rohling, E. J., Marino, G., & Grant, K. M. (2015). Mediterranean climate and oceanography, and the periodic development of anoxic events (sapropels). *Earth-Science Reviews*, *143*, 62–97. https://doi.org/10.1016/j.earscirev.2015.01.008

Rolandi, G., Bellucci, F., Heizler, M. T., Belkin, H. E., & De Vivo, B. (2003). Tectonic controls on the genesis of ignimbrites from the Campanian Volcanic Zone, southern Italy. *Mineralogy and Petrology*, *79*(1–2), 3–31. https://doi.org/10.1007/s00710-003-0014-4

Rooney, T. O., Bastow, I. D., Fontijn, K., Mariita, N., Muirhead, J. D., & Keir, D. (2025). The East African Rift System. In *Extensional tectonics: Rifting and continental extension* (Vol. 2, pp. 21–54).

Rowland, J. V., Wilson, C. J., & Gravley, D. M. (2010). Spatial and temporal variations in magma-assisted rifting, Taupo Volcanic Zone, New Zealand. *Journal of Volcanology and Geothermal Research*, *190*(1–2), 89–108. https://doi.org/10.1016/j.jvolgeores.2009.05.004

Royden, L. H., & Papanikolaou, D. J. (2011). Slab segmentation and late Cenozoic disruption of the Hellenic arc. *Geochemistry, Geophysics, Geosystems*, *12*(3). https://doi.org/10.1029/2010gc003280

Rubin, A. M. (1992). Dike-induced faulting and graben subsidence in volcanic rift zones. *Journal of Geophysical Research*, *97*(B2), 1839–1858. https://doi.org/10.1029/91jb02170

Rubin, A. M., & Pollard, D. D. (1988). Dike-induced faulting in rift zones of Iceland and Afar. *Geology*, *16*(5), 413–417. https://doi.org/10.1130/0091-7613(1988)016<0413:difirz>2.3.co;2

Ruppel, C. (1995). Extensional processes in continental lithosphere. *Journal of Geophysical Research*, *100*(B12), 24187–24215. https://doi.org/10.1029/95jb02955

Schattner, U. (2010). What triggered the early-to-mid Pleistocene tectonic transition across the entire eastern Mediterranean? *Earth and Planetary Science Letters*, *289*(3–4), 539–548. https://doi.org/10.1016/j.epsl.2009.11.048

Schmid, F., Petersen, G., Hooft, E., Paulatto, M., Chrapkiewicz, K., Hensch, M., & Dahm, T. (2022). Heralds of future volcanism: Swarms of microseismicity beneath the submarine Kolumbo volcano indicate opening of near-vertical fractures exploited by ascending melts. *Geochemistry, Geophysics, Geosystems*, *23*(7), e2022GC010420. https://doi.org/10.1029/2022gc010420

Smith, P. E., York, D., Chen, Y., & Evensen, N. M. (1996). Single crystal ^{40}Ar-^{39}Ar dating of a Late Quaternary paroxysm on Kos, Greece: Concordance of terrestrial and marine ages. *Geophysical Research Letters*, *23*(21), 3047–3050. https://doi.org/10.1029/96gl02759

Sparks, R. S. J., Annen, C., Blundy, J. D., Cashman, K. V., Rust, A. C., & Jackson, M. D. (2019). Formation and dynamics of magma reservoirs. *Philosophical Transactions of the Royal Society A: Mathematical, Physical and Engineering Sciences*, *377*(2139), 20180019. https://doi.org/10.1098/rsta.2018.0019

Stern, R. J. (2002). Subduction zones. *Reviews of geophysics*, *40*(4), 3-1–3-38. https://doi.org/10.1029/2001rg000108

Sternai, P. (2020). Surface processes forcing on extensional rock melting. *Scientific Reports*, *10*(1), 7711. https://doi.org/10.1038/s41598-020-63920-w

Svadlenak, H., Parnell-Turner, R., & Morris, M. (2026). A global evaluation of lithology-dependent marine sediment compaction parameters and their uncertainties. *Geochemistry, Geophysics, Geosystems*, *27*(3), e2025GC012739. https://doi.org/10.1029/2025gc012739

Thierry, S., Dick, S., George, S., Benoit, L., & Cyrille, P. (2019). EMODnet Bathymetry a compilation of bathymetric data in the European waters. In*OCEANS 2019-Marseille* (pp. 1–7). IEEE.

Ulvrova, M., Paris, R., Nomikou, P., Kelfoun, K., Leibrandt, S., Tappin, D. R., & McCoy, F. W. (2016). Source of the tsunami generated by the 1650 AD eruption of Kolumbo submarine volcano (Aegean Sea, Greece). *Journal of Volcanology and Geothermal Research*, *321*, 125–139. https://doi.org/10.1016/j.jvolgeores.2016.04.034

Valentine, G. A., & Perry, F. V. (2007). Tectonically controlled, time-predictable basaltic volcanism from a lithospheric mantle source (central Basin and Range Province, USA). *Earth and Planetary Science Letters*, *261*(1–2), 201–216. https://doi.org/10.1016/j.epsl.2007.06.029

Van Hinsbergen, D. J., Krijgsman, W., Langereis, C. G., Cornée, J. J., Duermeijer, C. E., & Van Vugt, N. (2007). Discrete Plio-Pleistocene phases of tilting and counterclockwise rotation in the southeastern Aegean arc (Rhodos, Greece): early Pliocene formation of the south Aegean left-lateral strike-slip system. *Journal of the Geological Society*, *164*(6), 1133–1144. https://doi.org/10.1144/0016-76492006-061

van Hinsbergen, D. J., & Schmid, S. M. (2012). Map view restoration of Aegean–west Anatolian accretion and extension since the Eocene. *Tectonics*, *31*(5). https://doi.org/10.1029/2012tc003132

Verroios, S., & Zygouri, V. (2021). Geomorphological Analysis of Xilokastro Fault, Central Gulf of Corinth, Greece. *Geosciences*, *11*(12), 516. https://doi.org/10.3390/geosciences11120516

Vougioukalakis, G. E., Laurenzi, M. A., Mastroianni, F., Schaen, A. J., Koutroulli, A., Kanellopoulos, C., & Francalanci, L. (2025). ^{40}Ar-^{39}Ar dating and new geological data to uncover the structure and evolution of the Kolumbo submarine volcanic field, Greece. *Bulletin of Volcanology*, *87*(11), 96. https://doi.org/10.1007/s00445-025-01873-6

Vroon, P. Z., Beemster, T., Zhou, X., Nomikou, P., Klaver, M., Wijbrans, J. R., & Kuiper, K. F. (2025). ^{40}Ar/^{39}Ar constraints on the eruption history of the Christiana Volcano of the Christiana-Santorini-Kolumbo volcanic field, Greece. *EGUsphere*, *2025*, 1–27.

Weinberg, R. F., Vernon, R. H., & Schmeling, H. (2021). Processes in mushes and their role in the differentiation of granitic rocks. *Earth-Science Reviews*, *220*, 103665. https://doi.org/10.1016/j.earscirev.2021.103665

Wilson, C. J., Gravley, D. M., Leonard, G. S., & Rowland, J. V. (2009). Volcanism in the central Taupo Volcanic Zone, New Zealand: Tempo, styles and controls.

Wulf, S., Keller, J., Satow, C., Gertisser, R., Kraml, M., Grant, K. M., et al. (2020). Advancing Santorini's tephrostratigraphy: New glass geochemical data and improved marine-terrestrial tephra correlations for the past∼ 360 kyrs. *Earth-Science Reviews*, *200*, 102964. https://doi.org/10.1016/j.earscirev.2019.102964

Zhu, L., Mitchell, B. J., Akyol, N., Cemen, I., & Kekovali, K. (2006). Crustal thickness variations in the Aegean region and implications for the extension of continental crust. *Journal of Geophysical Research*, *111*(B1). https://doi.org/10.1029/2005jb003770